Fluorescence Angular Domain Imaging with Stabilized Intralipid Test Phantom

by

Rongen Cheng

B.A.Sc. (Hons.), Simon Fraser University, 2009

Thesis Submitted in Partial Fulfilment
of the Requirements for the Degree of

Master of Applied Science

in the
School of Engineering Science
Faculty of Applied Sciences

SIMON FRASER UNIVERSITY
Summer 2012

APPROVAL

Name: **Rongen Lok Kan Cheng**

Degree: **Master of Applied Science**

Title of Thesis: **Fluorescence Angular Domain Imaging with Stabilized Intralipid Test Phantom**

Examining Committee:

Chair: **Dr. Andrew H. Rawicz**, P. Eng
Professor
School of Engineering Science, SFU

Dr. Glenn H. Chapman, P. Eng
Senior Supervisor
Professor
School of Engineering Science, SFU

Dr. Marinko V. Sarunic, P. Eng
Supervisor
Assistant Professor
School of Engineering Science, SFU

Dr. Mirza Faisal Beg, P. Eng
Internal Examiner
Associate Professor
School of Engineering Science, SFU

Date Defended/Approved: _____

Partial Copyright Licence

Abstract

Optical imaging through biological tissue has the significant challenge of scattering which degrades the image resolution and quality. Angular Domain Imaging (ADI) improves image quality by filtering out the scattered light in the biological tissue images based on the angular direction of photons. Using a newly developed solid fluorescing scattering phantom (SR = 17000, μ_s' = 48.4cm^{-1}), this allows us to couple ADI with conventional fluorescence imaging technique. We created a new solid phantom which mimics human skin tissue with a patterned fluorescing collagen layer. These phantoms have stability over 6 months, much longer than traditional tissue phantoms. Monte Carlo simulations analyzed the angular filtration performance with the new low aspect ratio 2D-Collimating Arrays (2D-AFA) under shallow scattering depth fluorescing scenario. Applying the ADI filters, 2D-AFA and SpatioFrequency Filter (SFF), to the scattering sample, we detected resolution targets (200µm - 400µm) embedded inside the medium.

Keywords: Optical Tomography; optical scattering imaging; Angular Domain Imaging; Fluorescence; Optical Monte Carlo Simulations; scattering tissue phantoms

Acknowledgements

I would like to thank my supervisor, Dr. Glenn H. Chapman, for his guidance, support and patience through my bachelor and master's theses work. Also, I would like to take this opportunity to acknowledge the research team at Simon Fraser University, Paulman Chan, Polly Tsui, James Dykes, Reza Qarehbaghi, Gary Chiang, and people who helped, advised, and worked with me on during the experiments. I would like to thank my committee members, Dr. Marinko V. Sarunic and Dr. Mirza Faisal Beg for their participation and direction on my project.

At last, I would like to thank my family and friends who provided encouragement and support during these years of study, and made this possible.

Table of Contents

Lists of Figures

Lists of Tables

Abbreviations

ADI:	Angular Domain Imaging
OT:	Optical Tomography
UV:	Ultraviolet
NIR:	Near Infrared
SR:	Scattering Ratio
TD:	Time Domain
OCT:	Optical Coherence Tomography
AFA:	Angular Filter Array
SFF:	SpatioFrequency Filter
2D-AFA	2D-Collimating array
MTF:	Modulation Transfer Function

Chapter 1: Introduction

Seeing through a medium with a high level of scattering creates a challenge in optical imaging. Due to a substantial amount of noise which is contributed by the scattered light present in the picture, different imaging techniques have been used or studied to tackle this problem. Although, there is not a significant impact when imaging through a low scattering level, for biological tissues, medium to high scattering levels are commonly found.

Typical optical medical imaging techniques are to capture a two dimensional image of the shadows which are created by the illumination of the tissue by a light source and the absorption in certain tissue layers. In an ideal scenario, the result is produced by projecting a beam of collimated light which projects into the medium and only the non-absorbed light is captured by the image sensor. When seeing through a scattering medium, photons from the projected collimated light interact with the tissue which causes a large portion of the light to be scattered. This scattering creates background noise in the shadowgram. As the medium's scattering level increases, the fraction of the light, which does not scatter, decreases exponentially. For example, a typical 1-mm thick of skin tissue has a scattering level of 20 scattered photons to 1 non-scattered photon (1). By eliminating the scattering photons entering the image sensor, we can improve the overall imaging quality. Several optical imaging techniques can be applied to eliminate or reduce the scattered light.

Traditional medical diagnostic tools such as X-Rays and Magnetic Resonance Imaging (MRI) are very useful when imaging through body (very thick tissue) with no tissue scattering effect. Also, they generate a high resolution result. Unfortunately, there are several disadvantages over optical imaging such as radiation induced tissue damage (for X-Rays) (2), high manufacturing, operating, and computing cost, restrictions of certain types of patients (patients with metal implants are not suitable for MRI). This leads us to have an optical imaging system which can image through scattering without tissue damage.

In contrast, optical imaging is generally safe if the illumination source is within the near ultraviolet (UV) to near-infrared (NIR) spectrum (3). Wavelengths in this range are non-

ionizing and do not damage biological specimens when using a modest intensity exposure (~4W/cm^2). Also, tissues characteristics, absorption and scattering, are wavelength sensitive which allow us to use a range of wavelengths to analyze tissue's physical and chemical properties. Thirdly, as technologies progress, the cost of quality illumination source such as lasers or high power narrow wavelength band LEDs are offered at modest cost. Finally, we can take the advantage of the fluoresencing properties of biological tissue such as the autofluorescence of collagen layer under skin as illumination source which can be used towards on other types of application.

As mentioned previously, background noise created by the scattering light from biological tissue is one of the major problems when imaging through tissue. When light enters a tissue, a large proportion of photons experience scattering events. In soft tissues, there are billions photons experiencing scattering events to each photon which passes straight through the tissue after a distance of few millimeters. These events create a high scattered to non-scattered light ratio that make it difficult to resolve an accurate image. For Optical Tomography (OT), literature has shown that a scattered to non-scattered photon ratio of 10^{11}:1, which can be interpreted as noise-to-signal ratio, as a possible ratio for successful image detection through a 5 cm thickness of human breast tissue (4). This poses one of the greatest challenges towards optical imaging through biological tissue which it is highly scattered; finding the technique to reduce or eliminate the scattered photons could significantly increase the signal-to-noise ratio in the resulting image.

Furthermore, most experiments in bio-optical imaging use different forms of tissue phantom which mimics the physical and optical characteristics of targeted biological tissues. Unfortunately, it is not easy to produce a stable, easy to handle, biological tissue phantom which maintains its optical characteristics overtime. This is especially important when a person wants to experiment several optical setups with a known, stable scattering phantom. A stable phantom would be extremely beneficial to medical image research field as tremendous amount of time and money would be saved on recreating and recalibrating a testing phantom for imaging purposes.

This thesis extends research on Optical Tomography (OT) technique for imaging shallow thickness scattering medium with fluorescence source illumination with Angular Domain

Imaging (ADI) by using a 2D-collimating array (2D-AFA) or a SpatioFrequency Filter (SFF) to eliminate scattered photons based on photon's trajectory. Another aim of this work is exploration on the creation of a solid, stable scattering test phantom. Combining these two major works, these allow us to show how effective is the applying ADI to shallow tissue thickness, and the performance of such newly developed phantoms.

This introductory section will discuss the theory and background of Optical Tomography (OT). Also various techniques on OT will be presented along with the explanation of objective of this research project.

1.1 Optical Tomography

Picturing through a scattering medium with light sources and optics to obtain internal structural information is called Optical Tomography (OT). Different OT techniques have been explored extensively in different fields of biomedical imaging and dialogistic applications. Since biological tissue is mostly highly scattering, a large portion of the incident light that exits the scattering medium differs from its original pathway. When a photon’s position diverts from its entering position, this creates scattered light, or in general, noise in the resulting image. Hence, it is important to increase the signal-to-noise ratio of the imaging method by eliminating/reducing the amount of scattering photons (noise) entering the image sensing mechanism. By understanding the photon transmission mechanism, it is beneficial to define an OT technique to increase the signal-to-noise ratio. In the following subsections, a discussion on photons transmission and several OT techniques is presented.

1.1.1 Photons Transmission

In general, optical tomography (OT) techniques depend on the fact that light often is weakly absorbed and can penetrate deeply into tissue, where some photons are absorbed but most are heavily scattered. For example, in an ideal scenario, when a collimated beam with an area (Ω) enters a medium, the exiting beam size remains unchanged (Ω) at the exit plane. This demonstrated that all the collimated photons have passed through the medium undisturbed. Hence, all photons are carrying information, which are called ballistic photon, travelled towards the imaging plane. Unfortunately, all biological tissues are turbid mediums where photons are likely to be scattered. To successfully obtain tissue information from the scattered light, ballistic or quasi-ballistic photons need to be separated from noise/scattered photons as shown in Figure 1-1

assuming to parallel surfaces on the medium. Ballistic photons enter and exit straight through the scattering medium along its original trajectory. Similar to ballistic photons, quasi-ballistic photons exit the scattering medium with minimal deviation due to scattering and their exit angle is relative small to the normal of the plane. On the other hand, scattered photons encounter a number of scattering events which remove almost all useful information about the tissue structure and this type of photon also introduces noise to the resulting image. To study the physical behavior of the photon pathway, there are several mathematical expressions to describe this scenario.

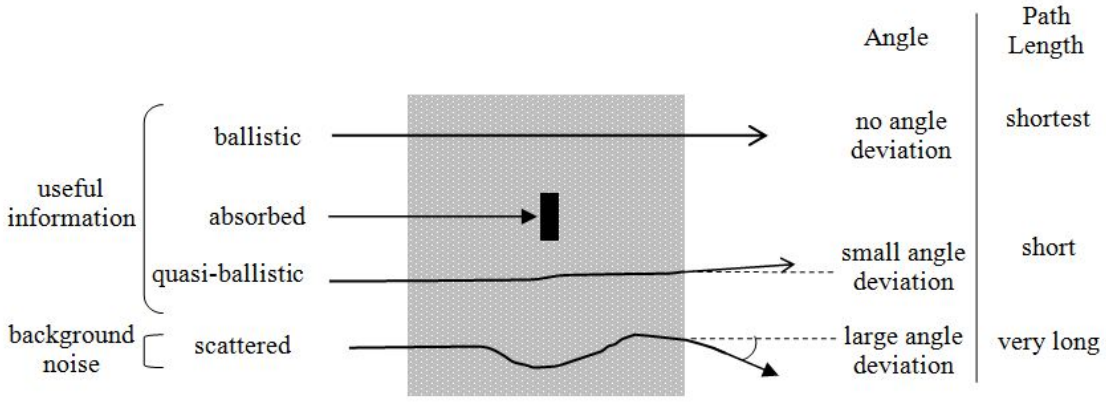

Figure 1-1: Photons transmission into scattering medium

1.1.2 Mathematical model on Optical Scattering

In biophotonics, several concepts have been applied towards photon's motion. Assuming no energy change during scattering event, most of the optical scattering under visible wavelength is considered as elastic scattering. Also, photon transmission in biological tissues is categorized by a few major factors. Most importantly, these factors are anisotropy factor, scattering coefficient, and absorption coefficient. First, the scattering coefficient and absorption coefficient is introduced by Beer-Lambert law [1]. From Beer–Lambert law, as a first approximation, we know that the intensity (I) of transmitted light decreases exponentially based on the absorption (μ_a), scattering (μ_s) coefficients, and tissue thickness (z).

$$I(z) = I_o e^{-(\mu_a+\mu_s)z} \quad [1]$$

Typically the absorption coefficient of human skin tissue (dermis) at 633nm (red light) is $\mu_a \approx 0.27mm^{-1}$ and the scattering coefficient $\mu_s \approx 30\ mm^{-1}$ (1). As showed in the Beer-

Lambert Law, both absorption and scattering coefficient are the exponential factor of the equation. This shows that if the scattering is much higher than the absorption, scattering becomes the dominant factor to the Beer-Lambert Law as well as to the turbid medium. From the previous example, for dermis the scattering coefficient is roughly 100 times higher than the absorption which the effect of the absorption is almost negligible compared to the scattering effect on the imaging applications.

1.1.3 Anisotropy in Tissues

When a photon hits a particle which triggers a scattering event, the photon then travels at a deflected angle from its original pathway as in figure 1-2. This angle is defined as scattering angle.

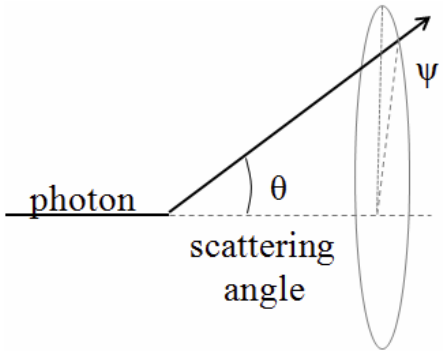

Figure 1-2: Deflected photon after a scattering event

After a scattering event which caused by a particle, the photon deflects by an angle θ along its original trajectory, and rotated by an angle ψ. Anisotropy is defined as the mean value of the cosine value of the deflection angle, θ. This leads to the definition of anisotropy factor, g, which can be expressed mathematically in the equation [2].

Generally, in tissues, light tends to have a strong forward scattering. Hence, tissue scattering is anisotropic. To mathematically describe this behavior in tissue, the Henyey-Greenstein function allows us to determine the phase angle probability distribution of a photon at different anisotropy factors by:

$$p(cos\theta) = \frac{1}{2}\frac{1-g^2}{(1+g^2-2gcos\theta)^{3/2}} \quad [2]$$

where at the extreme ends:

- g = 0 – isotropic (uniform scattering in all directions)
- g = 1 – completely forward scattering
- g = -1 – completely backward scattering

Normally, anisotropy factor (g factor) measures by experiment on specific tissues. In human tissue, g ranges from 0.75-0.95 for soft tissues, and for human dermis this value is about g = 0.819 (1). This value shows that soft human tissues are highly forward scattered, hence it significantly reduces the number of backward scattered events.

Due to the fact the human soft tissue are highly forward scattered, it reduces the scattering coefficient in tissue. This allows us to determine the reduced scattering coefficient (μ_s') by combining scattering coefficient and isotropy factor. The reduced scattering coefficient (μ_s') which better represents the transmitted light. Reduced scattering coefficient is defined as:

$$\mu_s' = \mu_s(1 - g) \quad [3]$$

Combining the anisotropy and scattering theory, the reduced scattering coefficient is a better representation of photon scattering behavior in human soft tissues. With a g factor of soft tissues of typically ~0.75-0.95, this reduces the scattering coefficient by 75%-95% which substantially improves the ratio of information-carried photon to noise-carried photon.

1.1.4 Scattering Ratio

To standardize our system performance, we used scattering ratio (SR) to denote as the ratio of scattered to non-scattered light. From Beer–Lambert law (equation 1), we can mathematically express this ratio in follow:

$$SR = \frac{I_o}{I_{bq}} - 1 = e^{(\mu_a + \mu_s')z} \quad [4]$$

where I_o is the initial light intensity and I_{bq} is the combined ballistic and quasi-ballistic light intensity. For example, a 1-mm thick of human skin tissue has a SR of roughly 5:1 based on the value presented in 1.1.2 and 1.1.3.

1.2 Optical Tomography Techniques

To extract an image from a highly scattered medium, several different OT techniques are being investigated. In most other research, these approaches are based on either a photon's path length or photon's trajectory when passing through the medium. Two commonly used ones are Time Domain (TD) and Optical Coherence Tomography (OCT) are based on discriminating scattered and non-scattered photon's path length when it passes through a scattering medium. On the other hand, Angular Domain Imaging (ADI) used in this work filters these photons based on their trajectory and exit angle from the medium (4). In the next section we will compare these methods.

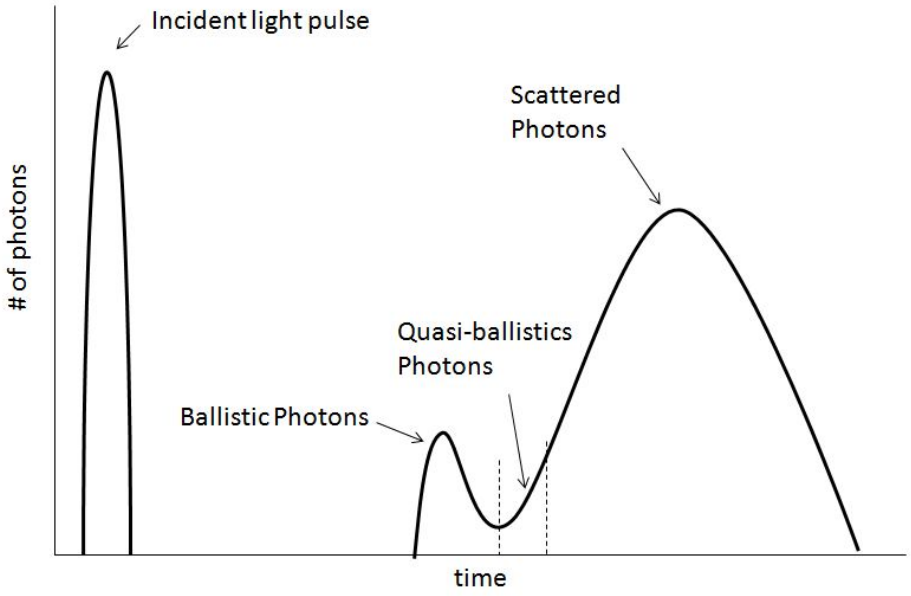

Figure 1-3: Photons distribution after scattering medium in time domain

1.2.1 Time Domain (TD) and Optical Coherence Tomography (OCT)

Although Time Domain and Optical Coherence Tomography are based on photon's path length, these two methods have a different approach on scattered and non-scattered photon detection. TD assumes ballistic and quasi-ballistic photons have the shortest paths through the turbid medium compared to highly scattered light. As shown in figure 1-2, when a pulse of incident beam enters a scattering medium, the ballistic photons exit the medium with the shortest path. Hence, these photons are the first being seen at the sensor. The numbers of undisturbed photons is significantly lesser than quasi-ballistic and scattered photons as in figure 1-3. In order to produce a proper result by using time

domain method, a very fast response time-gated camera is required. A typical range for usable light pulse is in the order of Femtoseconds to get resolutions in the sub mm range which are expensive to the overall system (4). These are both expensive and difficult to set up.

By contrast OCT relies on interference effects to detect non-scattered photons by using a reference beam. The phase of the light is directly related to the path length. For ballistic and quasi-ballistic light, these will be in phase with a reference beam of the same optical path as the medium while scattered light will be out of phase. Comparing with Time Domain Tomography, OCT requires relatively less sophisticated equipments and it is capable of imaging at depth of 1 to 2 mm in most tissues (4), but it requires a reference path and interferometric detection.

1.3 Fluorescence Angular Domain Imaging (ADI) Concepts

When photons pass through a turbid medium, most are randomly scattered and thus exit at random angles, while the ballistic photons are unaltered as shown in figure 1-1. In ADI, after the medium, an angular filter is aligned in such a way that it rejects the scattered photons which are at angles different from the source and allows ballistic and quasi-ballistic photons which are close aligned to the source to continue. This filtration is defined by the limiting the photon's exit angles which is called the acceptance angle. The acceptance angle accepts a narrow cone of light which blocks out the high exit angle of scattered photons. Then, the filtered light is collected by a camera sensor to form an image of the sample and its internal structures (see figure 1-4). As shown, in order to successfully filter out the scattered photons from ballistic and quasi-ballistic ones, the scattering medium surface and angular filter must be carefully aligned.

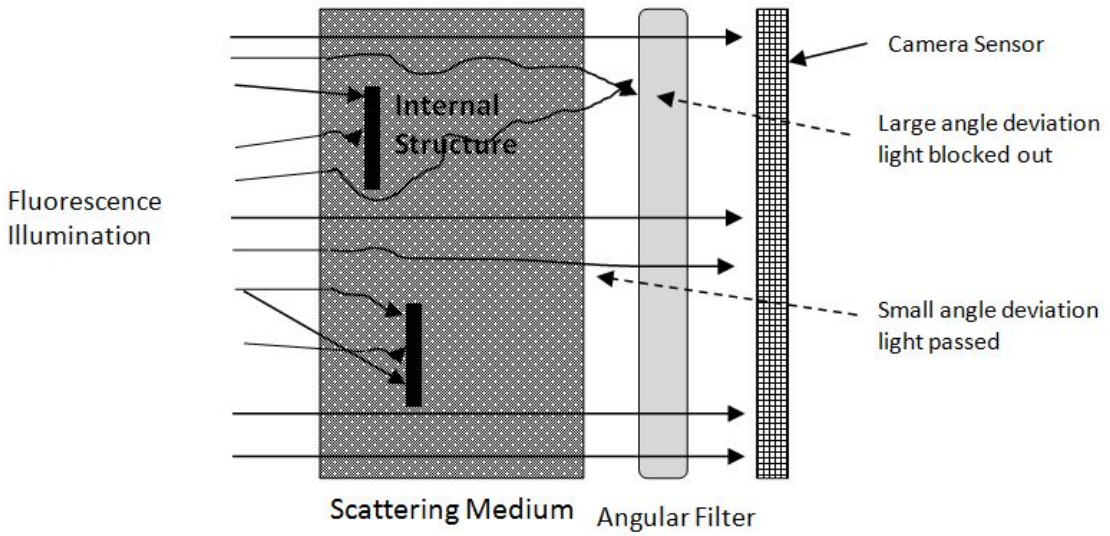

Figure 1-4: Trans-illumination ADI illustration

When scattered light has been filtered by the angular filter, the light detector will then only detect the ballistic and quasi-ballistic light. Hence, a typical optical sensor will fit this task as compare to sophisticated equipments required by TD and OCT techniques. Detail setup for ADI filtering system will be discussed in chapter 2.

1.4 Research Objective and Scope

Comparing this master thesis work with my previous bachelor thesis work that was focused on ADI with coherent light sources. This one was mainly focused on applying ADI to shallow scattering thickness in fluorescence settings. This thesis work applied Angular Domain Imaging systems (2D-collimating arrays and SpatioFrequency Filter) in shallow scattering thickness with fluorescence settings to understand the feasibility on applying ADI filtering systems in an inexpensive and non-invasive manner. The previous work in ADI research used a high power, expensive Argon ion laser or other types of diode laser sources on diluted milk samples for thick scattering phantoms. In these chapters, we will analyze the limitations and effectiveness of these ADI filters in different shallow scattering depth applications with fluorescence.

Also, previous work used either diluted milk or intralipid as a scattering phantom which held in liquid form. This posed problems when conducting experiments with this type of phantom. Since the phantom is in liquid form, the shape of the phantom limits by the shape of its container. Also, it does not easy to manipulate the sample in different orientations. This limits the optical setup which the test sample requires a dedicated

holder/stage when performing experiments. Furthermore, using an organic tissue sample in liquid form, it is prone to environmental effects which the changes in organics overtime changes its optical characteristics. The stability of the testing object is important. Otherwise, we need to constantly calibrate the phantom which makes it hard to compare result with experiments. This thesis has discovered a new technique on creating a long-lasting solid scattering phantom with long-term stability about its optical properties which aims to mimic human soft tissue. In the latter chapters, experiments also conducted on these newly created phantoms on our ADI systems to understand the overall performance towards a new state of scattering phantoms, i.e. from liquid state to solid state.

1.5 Thesis Organization

This first chapter contains an overview of the thesis and previous research, with an introduction on scattering theory, and the current optical tomography imaging methods.

Chapter two describes Angular Domain Imaging with fluorescence in details, and a discussion of the benefit with the application of scattered photon filtration, namely by applying Angular Domain Imaging as an enhancement. It also provides a discussion of the challenges and advantages of ADI.

Chapter three describes the creation of the solid scattering phantom with Intralipid. A detailed explanation and procedures required to produce the phantom will be discussed. Also, measurements of their optical properties and comparison are presented.

Chapter four presents the results of the simulations using a Monte-Carlo program of ADI fluorescence imaging. Results with different types of fluorescence source, such as plane source and injected source are discussed and analyzed.

Chapter five summarizes the results of the 2D-collimation array imaging system on chemically-etched glass as a shallow scattering medium with R6G infused plastic slide as plane fluorescence source and the imaging performance on this new 2D-collimation array at different scattering levels.

Chapter six discuss about the results of SpatioFrequency Filter on the solid scattering phantoms, and a small aquatic creatures. Results at varying scattering ratios are presented.

Chapter seven contains conclusions and ideas for future work on this research topic.

Chapter 2: Angular Domain Imaging (ADI) with Fluorescence

Angular Domain Imaging (ADI) is a technique to filter out the scattered light which creates a background noise obscuring the internal structure in a tissue. Since noisy photons exit a scattering medium with a wide range of angles, they can be filtered out by accepting only those with angles close to the original light pathway. Experiments carried for this research use the trans-illumination fluorescence technique where the excitation light source enters from one side of the medium to a fluorescence material which emits fluorescence light towards the medium and the detector positions on the other side. This chapter introduces and explains fluorescence ADI theory and concepts. By explaining this theory, it can be seen that an angular filter can sufficiently reduce most of the scattered photons that the information carrying ballistic/quasi-ballistic light becomes dominant and allows us to understand its limitation. In the following sections, we will be presenting the different components involved in the 2D-collimation array and SpatioFrequency Filter ADI which are our experimental systems setup.

2.1 Trans-illumination ADI with Injected Fluorophores

In this thesis, we will use both trans-illumination fluorescence (figure 1-4) and trans-illumination with injected fluorophores (figure 2-1) ADI where a scattering medium is illuminated by either an emission of fluorescence light from one side (figure 1-4) or a light excites the injected fluorophores to induce fluorescence emission within the medium (figure 2-1). Comparing with trans-illumination fluorescence ADI (figure 1-4), fluorescence light in the other setup (figure 2-1) is emitted in nearly uniformed directional ball of light which differs from directional collimated light of a laser. Since photons from fluorescence light are not collimated and the imaging sensor is a 2D sensor plane, this makes the informative ballistic and quasi-ballistic photons are harder to capture than in the regular trans-illumination ADI with collimated light in the previous work. The reduction of informative light in fluorescence means the overall image brightness of an image is lower than the image in collimated source. Hence, this poses a challenge towards our imaging system.

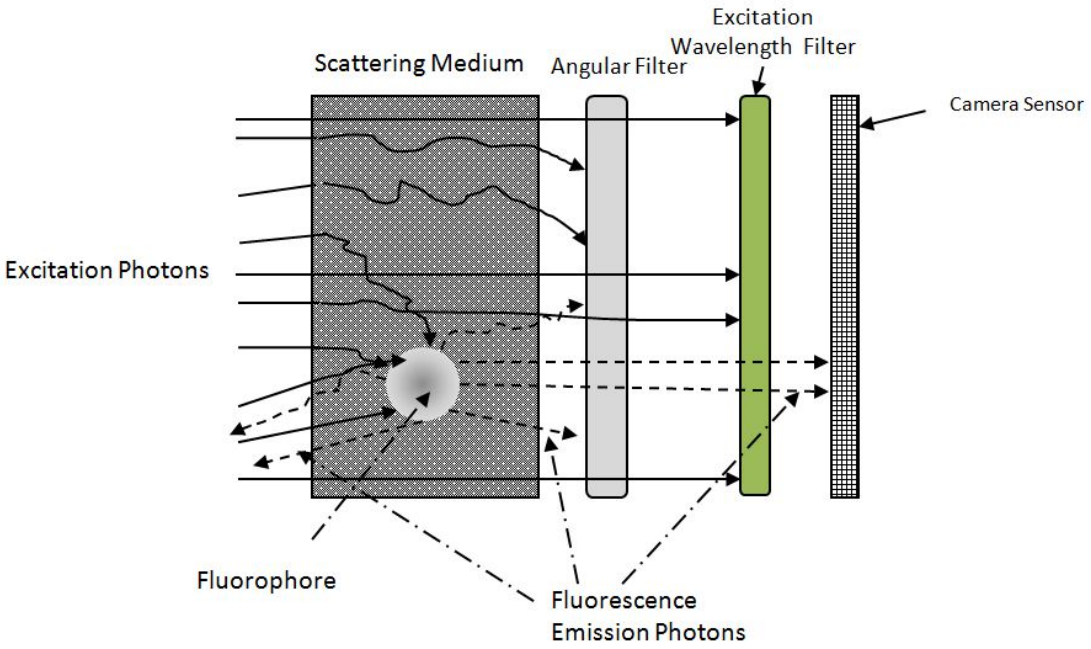

Figure 2-1: Trans-illumination with Inject Fluorophore ADI illustration

2.1.1 Fluorescence Imaging

Fluorescence is where a material absorbs light from an excitation wavelength and emits a longer wavelength. The shift in the fluorescence excitation and emission spectra is referred to as the Stokes Shift (figure 2-2) where the emission of the spectrum has a longer wavelength than the excitation light. Note that the light intensity emission spectrum of fluorescence is lower than the excitation's due to the efficiency of the fluorophores. In general, the autofluorescence which appears in nature tends to have a lower efficiency than artificial fluorophores. Thus, the light intensity of autofluorescence is lower.

With the shift towards the longer wavelength, this is an advantage in fluorescence imaging because a longer wavelength light source undergoes less scattering in biological specimens, and results in better resolution images than that can be achieved using shorter excitation wavelength light sources. The auto and induced fluorescence sources used in this experiment has an excitation at 415nm, and an emission spectrum between 555-585nm with a stoke shift of 155nm. Generally, injected fluorescence, which normally is artificially created, has higher emission intensity than autofluorescence, which exists in nature. Since we are using an excitation source which is not relevant to

fluorescence imaging, a wavelength filter is used to filter out the excitation light which distorts the picture quality.

By studying the autofluorescencing cells in tissue overtime which is difficult for OCT and TD as it has no coherence and requires long exposure while applicable on ADI, abnormal or cancerous behaviors can be detected and observed as the fluorescing patterns change. Because of its potential as a screening tool on cancerous cells, studies are being performed to facilitate the detection and diagnosis of cancers in various body parts. Currently, the imaging techniques utilize in fluorescence imaging often only uses simple optics imaging systems. Simple absorbing filters are used in these imaging systems to eliminate the undesired light source, such as the excitation light source and any unintentional fluorescing emission due to overlapping excitation spectrum. However, the scattering effect in tissue can contribute a significant amount of image degradation in relation to the depth of tissue being imaged. Although the impact of scattering is much less for shallow tissue imaging, as the depth increases, the uniformly direction emission from the fluorescence becomes the problem. Since ADI performs angular filters based on a selected axis plane, the emitted photons, which release in all directions uniformly, generates a large number of scattering photons compare to trans-illumination ADI (discussed in section 1-3). Hence, the background noise from scattered photons increases exponentially. By applying ADI to fluorescence imaging, we hope to improve the resolution of the fluorescent images that can be provided by the existing simple fluorescence imaging systems.

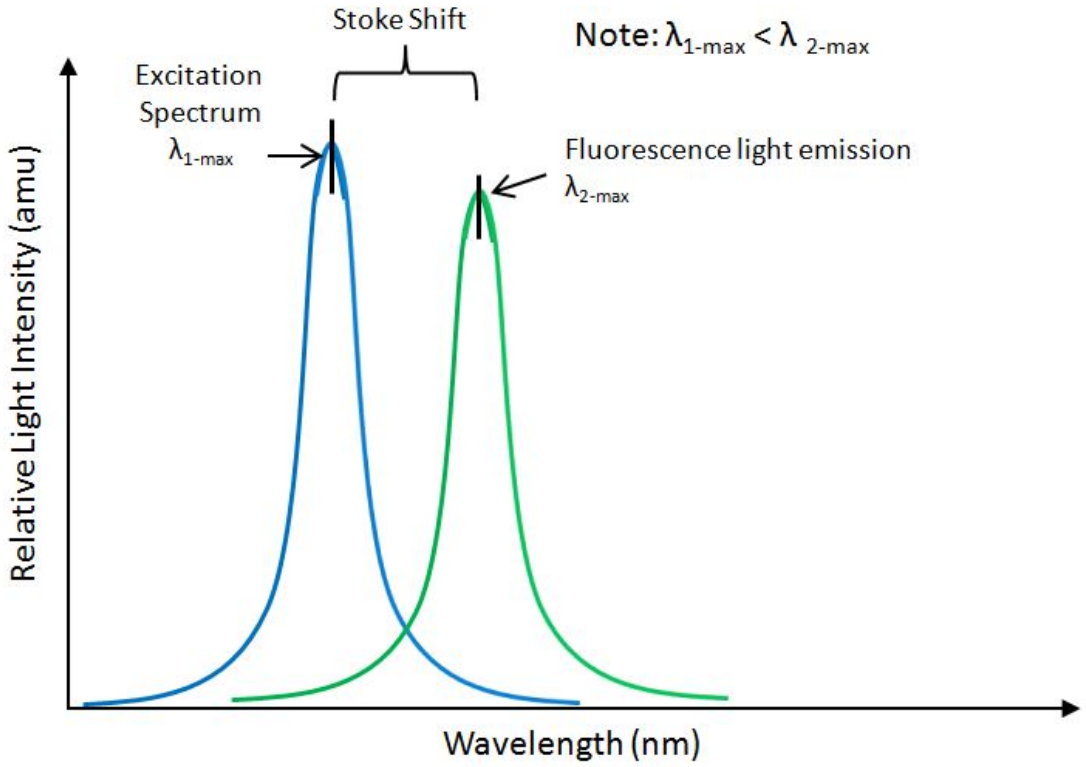

Figure 2-2: Example of a Stoke Shift in Fluorescence

One common example is the fluorescence of the collagen layer in skin. Collagen is a fluorescent layer located approximately 1mm underneath the epidermis; with an excitation spectrum of 340-470nm (UV to violet) and an emission spectrum of 420-540nm (blue to yellow) (5). Under normal condition, the fluorescence from collagen cells spreads out uniformly over the entire area however; fluorescence is very sensitive to the chemical and structural make up of the material. Research has shown that if there is a degradation in any collagen cell (e.g. cancer), the fluorescence phenomenon appears to disappear or decrease in intensity (5). By observing the dark spots in a fluorescence image, medical personnel can identify potential problematic areas and prevent the spreading of any problems.

Currently, one common setup for fluorescence imaging is confocal fluorescence microscopy. The specimen is imaged by exciting fluorescent cells at each focal plane of interest, and only light from that particular focal plane is collected due to the placement of a pin hole within the imaging device. This minimizes the signal to noise ratio. However, fluorescence confocal microscope has limited depth of focus, narrow field of

view, and restricted application for in-vivo specimens. However, combining fluorescence imaging with ADI, we can overcome such limitation which will be shown in the following chapters.

2.2 Angular Domain Imaging Concepts

Angular Domain Imaging is based on the difference exit angles of scattered and non-scattered light as illustrated in figure 1-1, non-scattered light has a small exit angle relative to the original light source compares to scattered light. Previous work with using Monte-Carlo simulation shows that photons with exit angle less than 0.5° have path length virtually identical to ballistic photons (6). Based on this simulation, an angular filter with small acceptance angle (< 0.5°) can help to filter out most of the scattered light from non-scattered light.

Acceptance angle is an angle that allows photons with no/small deviation from the horizontal path to pass through as in figure 2-3. Any other photons with a higher deviation angle than the acceptance angle, they will be blocked out. In previous work, a small array of tubes called Angular Filter Array (AFA) (figure 2-4) serves as an angular filter by having a small acceptance angle through which light passes (7). This angle can be calculated as follows:

$$Acceptance\ Angle = \tan^{-1}\left(\frac{51\mu m}{1cm}\right) = 0.2922° \quad [5]$$

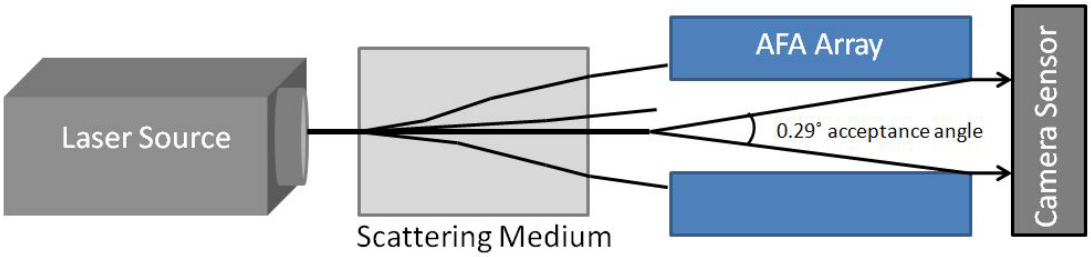

Figure 2-3: Acceptance Angle of AFA array (after Paulman (4))

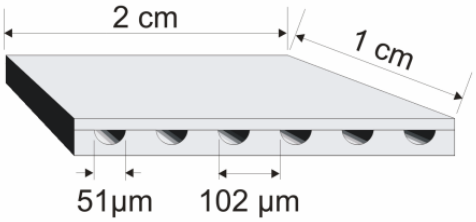

Figure 2-4: Linear Collimating Array (4)

2.2.1 2D-Collimating Arrays

In previous work, a single-line collimating array has used towards ADI system which called AFA (in figure 2-3 and 2-4). That particular collimating array has an aspect ratio of roughly 100:1 with an acceptance angle, $\theta_a \approx 0.572°$ which used in observing a 5-cm thick sample. In Angular Domain Imaging, the acceptance angle is used to express the filtration power of the ADI filters. The acceptance angle is calculated based on the diameter (Ø) of the holes, the length of the holes (l) as shown in equation [6]. For the single-lined collimating array, it produces a full field image by scanning the medium line-by-line. This is time consuming and prone to alignment errors. To tackle this problem, 2D-collimating array is designed and created to reduce the number of scans and as a proof of concept of creating a bigger matrix of array for ADI system.

$$\theta_a = 2tan^{-1}\left(\frac{Ø}{2l}\right) \quad \textbf{[6]}$$

Also, the AFA is designed for thick scattering medium in the range of few centimeters. It is designed to remove very high (>10^6) scattering ratio with a collimated source. For shallow scattering thickness, about few millimeters of scattering tissue, we decided to fabricate a collimating matrix with a lower aspect ratio. From the results of the Monte Carlo Simulation on shallow depth scattering thickness (which will be discussed in chapter 4), a collimating matrix with 10:1 aspect ratio is sufficient to provide angular photon filtration.

In order to fabricate such a collimator, a thin sheet of ABS plastic sheet with 0.85mm thickness is used. To maintain the 10:1 aspect ratio, the collimator holes have to be shrunk to around 80µm diameter. A 10 x 60 collimator holes array is fabricated at SFU with precision laser drilling of materials. Using this laser fabrication technique produced a collimator hole of 88µm diameter which gives an acceptance angle of 5.93º. Figure 2-5(a) is a microscopic image of the collimator array. It shows that the laser drilling created a slightly tapered (0.4^o) collimator as in figure 2-5(b). This is due to the depth of focus of the laser spot. Even though the collimator holes are not symmetrical on the horizontal axis, the angular filtration performance will not be affected as the acceptance angle is calculated from the end of the collimator holes. To ensure a proper

angular filtration during the experiment, the front side of the 2D collimating array needs to be places towards the scattering sample.

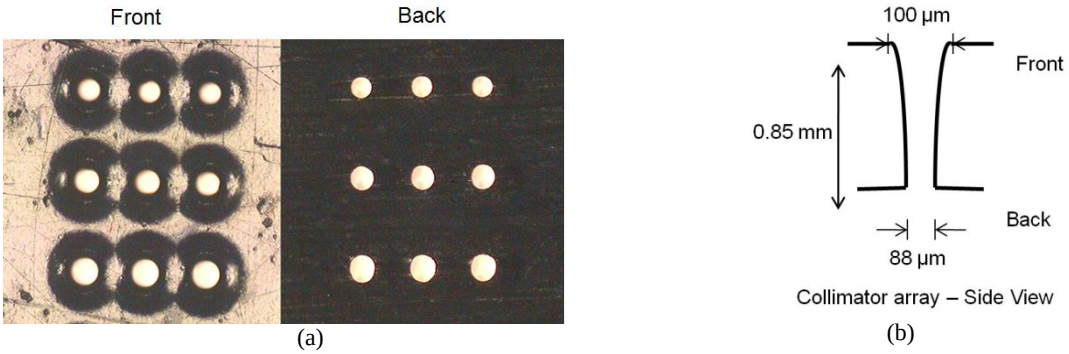

(a) (b)

Figure 2-5: 2D-Collimating Array (a) Top view (b) Side view

2.3 Aperture-based Spatio Filter ADI

Previous work with the use of the micromachined Angular Filter Array (AFA) (figure 1-4) in trans-illumination technique for imaging a scattering medium has achieved images with SR ratio to 10^6:1 with an acceptance angle of 0.29º (3) (4) (8). When using a 1-mm width thin line of light illumination, SR ratio of 10^8:1 can be reached. As an alternative ADI filter to the linear collimating array, the SpatioFrequency Filter (SFF) is introduced.

As mentioned, previous research concentrated on Angular Filters created from micromachined collimators. There are some limitations with this type of angular filter. The images must be built up from scanning the linear array over the area. Second, scanned image will have a series of dark spots which created by the spacing between each array tubes. Finally, the acceptance angle of the micromachined collimators is fixed. If we want a specific acceptance angle, the physical dimension of the filter has to be changed its diameter and a new filter fabrication.

The concept of the SFF is to create an alternative aperture-based spatio Filter implemented by using a converging lens and aperture placing near its focal point to limit the acceptance angle where the distance between the SFF system and the scattering medium should be minimal (see figure 2-6). The theory behind SFF is that the radial distance of a photon upon entering the system is dependent on its trajectory and the

converging lens focal length, thus allowing the pinhole aperture to reject any photon with a radial distance greater than the aperture radius. Using the setup, a trajectory filtration angle is created by the combination of the lens' focal length (f) and the size of the aperture holes (Ø). In ADI, the filtration angle is defined as acceptance angle (θ_a).

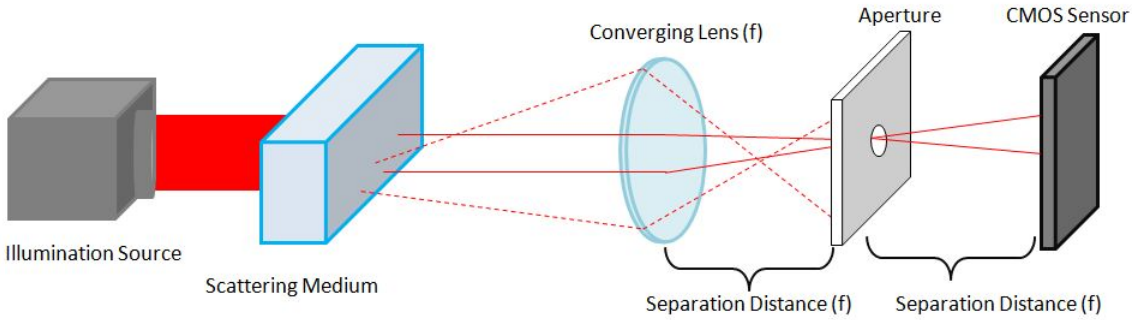

Figure 2-6: SFF system with lens, aperture, and imaging sensor

The components and setup of the SFF system presents four limiting factors to the image resolution: the lens focal length *f*, the image sensor position (usually at 2f), the aperture diameter ϕ and the degree of trajectory filtration. The resulting acceptance angle θ_a is given by

$$\theta_a = 2\tan^{-1}\left(\frac{\emptyset}{2f}\right) \quad [7]$$

Previous work showed that the smallest useful angle is caused by Rayleigh criterion for the diffraction-limited resolution (4) (9). When an aperture size is smaller than 100µm, diffraction effects dominate in the picture. For example in figure 2-7, when a collimated laser source pass through an small aperture, diffraction patterns can be seen. Thus, the overall image will be heavily distorted by this pattern overlaying the result. This diffraction is due to the circular effectively Airy diffraction which can be shown mathematically in equation [8]. The optimum resolution tradeoff was found to be by setting equal aperture and trajectory resolutions. The setup in this thesis is going to use a 500µm, a 300µm, and a 150µm aperture, +75mm lens, ~0.38°, ~0.23°, and ~0.12° trajectory filtration, and sensor at the converging lens' focal length to aperture. Since the SFF provided a full view image filtration, unlike other ADI techniques, images can be captured in real-time at rates which are only limited by the CMOS Sensor. Inherently, as the aperture introduced into the system, the total amount of light reaches the CMOS

Sensor is reduced. Hence, a long exposure could be required for a highly scattered medium.

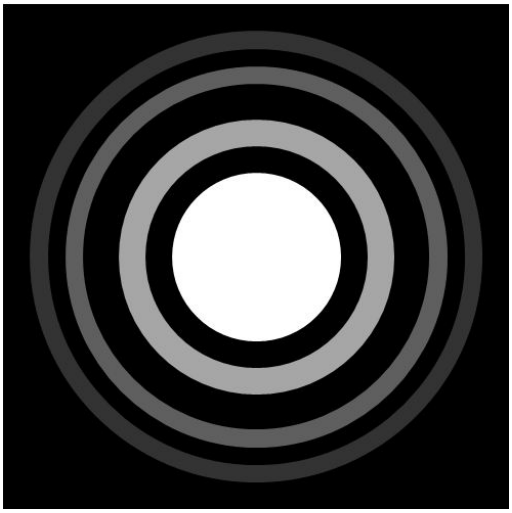

Figure 2-7: Images of collimated laser source passes through a 100μm aperture

$$d_{min} = \frac{2.44 f \lambda}{D} \quad \textbf{[8]}$$

In our previous research, using Monte Carlo simulations, it was demonstrated that the exit trajectory of quasi-ballistic photons has very little difference from the straight-line path taken by ballistic photons. Therefore; the SpatioFrequency filter can eliminate a majority of the scattered photon noise from the image.

2.4 Camera Sensor

To provide a full field imaging, the sensor used in this experiment is a 22.7mm x 15.1mm CMOS sensor from a Canon 10D DSLR camera and a Bayer color filter array configuration. This camera has 3072 horizontal by 2048 vertical pixel elements, and has a pixel size/resolution of 7.6μm (horizontally) by 7.6μm (vertically). The reason we used a commercially available camera sensor than a specific sensor for scientific research is because the commercial one (cost ~$300) provides a greater light sensitivity (ISO range up to 1600), cost lesser than scientific ones (cost > $10K), better software support which allows remote micro-adjustment such as exposure, ISO, image size, etc., larger image size (3027x2048 to 1024x768). With these advantages, a commercially available camera is the best choose for this type of imaging.

2.5 Measuring Image Quality

To obtain a measurement metric for the visibility of the phantom structure numerically, we can calculate the Modulation Transfer Function (MTF) of the scanned image. In general, MTF is defined by the below formula:

$$MTF = \frac{Imax - Imin}{Imax + Imin} \quad [9]$$

where I_{max}, I_{min} stand for maximum intensity and minimum intensity of the image. A higher MTF value allows us to distinguish the object from the background noise. Generally, MTF are commonly used to evaluate the quality of an imaging system. In ADI, pictures are taken with scattering medium and resolution targets in forms of lines-and-spaces. The scattering inherently will degrade/blur the image which affects the MTF. This makes the reduction of MTF in different images is mainly due to the scattering. Also, within the same image, the MTF for a larger lines-and-spaces target is higher than a small one. Hence, this allows us to study detectability limit of the optical system.

In general, when an image's MTF is below 0.03, we consider the object is at the detection limit and the test structure is indistinguishable from the background. This will become a guide for us to define the detection limit of our system. Figure 2-8 (a), (b), and (c) show the captured image as different MTF (10). We can clearly see the structures of the test phantoms at MTF = 0.7548, and can able to distinguish the structures in the image of MTF = 0.05787. But when MTF < 0.03 (figure 2-8 (c)), we are not able to visually detect the present of test structures. This shows the MTF = 0.03 is our bottom line of measurement.

(a) **(b)** **(c)**

Figure 2-8: Sample Scanned Image at MTF of (a) - 0.7548, (b) - 0.05787, (c) < 0.03 (10)

2.6 Chapter Conclusions

In this chapter, we discussed the theory behind angular domain imaging with fluorescence which is to filter out noise carrying photons, i.e. scattered photons, from the information carrying photons from a fluorescence source which emits from an excitation source. Hence, the challenge of using fluorescence compares to traditional ADI. Also, we described two different ADI filters, the 2D-Collimating Array and the aperture-based spatio filter, SpatioFrequency Filter ADI, and the calculation of theirs acceptance angle.

In next chapter, the solid scattering phantom with Intralipid will be discussed. Creating a solid 3D scattering phantom from polymer casting technique, it allows us to have a long term reusable scattering phantom towards different experiment system which is not limited to ADI systems. Furthermore, an in-depth analysis on the stability of its optical properties is presented.

Chapter 3: Intralipid-infused Solid Tissue Phantoms

In this chapter, we describe a new tissue phantom which meant to be suitable for any types of OT imaging setup for example, ADI, OCT, TD or microscopy. Instead of conventional tissue phantom which only lasted for few days, this scattering phantom is created to maintain its optical characteristics over an extended period of time. In order to create a long last solid tissue phantom, multiple fabrication steps and techniques are incorporated from other research works. Furthermore, with the success of these new fabrication procedures, we are allowed to create a more complicated artificial phantom such as multi-layered tissue, different fluorescent layers, shape, etc.

3.1 Intralipid as Scattering Phantom

Making stable complex optical scattering phantoms that mimic tissue behavior is a long standing problem in this type of research. To create a controllable, calibrated scattering medium to mimic human soft tissue, liquid Intralipid has been used extensively in research (3) (11-20). Intralipid, which its main ingredients are soybean oil, egg phospholipids, and glycerin, is a nutrient supplement for patients. It has a similar optical characteristic as human soft tissues with anisotropy factor (g) roughly around 0.75 – 0.85 depending on manufacturer, and its scattering coefficient can be easily adjusted based on its dilution in several substances (10). Thus, it is convenient to create different scattering tissue thickness via Intralipid diluted in water. For previous work in ADI, we have been using a range of diluted Intralipid concentrations and thickness to serve as scattering phantoms in liquid form. The problem with intralipid solution is that is an organic material which it decays at room temperature within a day and it is difficult to form into complex shape with its liquid state. Thus, the phantom shape is solely relies on the shape of the container.

It is problematic to experiment with an organic material in vitro. When an organic material decays, its optical properties changes dramatically which requires a new calibration of the scattering sample every time a new test structure is created or used. This makes doing several experiments on the same test structure with different setups difficult as the usable period of the sample is short due to the deterioration of the material. Also, it limits the repeatability of the experiment and makes the comparison of different measurement methods difficult. Although a phantom requires some calibration

and handling precautions, it has an enormous advantage. This does not involve living animal. When using a living animal as an experiment subject, it requires a lot of extra lab handling conditions and costs just to handle the animal.

Also, employing an actual living tissue for experiment, the variation in sample makes problems when standardizing the results. Furthermore, health and safety protocols and limitations are necessary for testing on animals. For example, a separate permission is required for different wavelength used in the experiment. Therefore, using a scattering phantom in vitro is still preferred in experiments.

3.2 Non-Intralipid Solid Scattering Phantoms

As discussed in above section, a scattering phantom made via organics is prone to degradation. Papers in the literature have used many different types of new materials and forms for test phantoms such as a quartz glass spheres (radius of ~250nm) suspense in water (11), amorphous silica spheres (radius ~500nm) casted in clear plastic (12), TiO_2 powder with 2-3μm particle size casted in clear plastic (13). Although these materials are able to create a stable scattering medium, it requires extra work on finding the optimal value for each parameter, such as the refractive index of the materials, wavelength absorption and scattering characteristics, in order to produce a workable phantom. Intralipid, on the other hand, has been extensively used in scattering imaging research since 1990 (14) and has been very well characterized since then. To take the advantage on this well understand material, we decided to explore a new way to create scattering phantom from intralipid solution.

3.3 Intralipid-infused Agar Fabrication

Since diluted intralipid has a short lifetime (less than one day) (4), we want to extend the intralipid's lifetime as a long term usable phantom. Existing research has experimented with infusing intralipid solution into agar which creates a solid scattering medium while maintaining intralipid's optical characteristics. (15) (16) The inspiration for this technique of the intralipid infused agar starts with the work of Cubeddu, et al. (16). The idea of using infusing the agar with intralipid solution is to use the agar as a medium container which creates a solid structure with homogenous mixture.

Laboratory grade agar powder from Anachemia and 20%-Intralipid solution from Fresenius Kabi have been used for the solid scattering phantom creation. For this research, we used a 1% agar concentration with various intralipid concentration solutions which are diluted by using deionized water. The agar is warmed up to around 60°C to ensure agar powder has dissolved completely. When the agar solution cools down to roughly 40°C, we mixed in the intralipid solution and poured the mixture into a mould. The solid intralipid-infused agar will be set, depending on the thickness, normally in less than 24 hours at room temperature. Since agar is in a liquid form before it completely sets into solid, we can easily mix the desired concentration of intralipid solution into the agar mixture. Hence, different scattering ratios can be achieved. The key to this method is that both agar and intralipid are compatible organics that are diluted in water Also, it is important to know that the mixture can then be formed into any shapes theoretically based on the shapes of the mould as shown in figure 3-1 that a thick layer of agar is formed on a circular disk shape.

Figure 3-1: Intralipid Infused Agar on Glass

3.3.1 Agar Shrinkage Problem

There are multiple benefits on creating a solid scattering phantom. First, it can be formed into any shapes/geometries based on the experimental needs. Secondly, in principle the solidity of the phantom allows us to manipulate it in many orientations while maintaining its homogenous scattering characteristics which are important as we discussed in previous section. This property is hard to achieve with the liquid form of phantoms. Furthermore, from our experiments and in the literature, we found that the intralipid infused agar extends the lifetime of the scattering phantoms from one day to around

three days depending on the temperature and the humidity of the environment. Unfortunately after three days, the solid agar phantom dries out rapidly into a thin sheet of material and self-peeled away from its container. This is due to the water content in the agar evaporating (Figure 3-2). As mentioned previously, the 3-days drying time is dependent on the temperature and humidity. If the environment is low in humidity, the drying time will be shortened. This problem agrees with other results in the literature (16) which indicates that only using intralipid-infused agar could not be a long term solution for creating a stable solid scattering phantom. In this chapter, our research will show a new concept of encapsulating the agar to create a stable, solid, and long lifetime fluorescence scattering phantoms for human soft tissue imaging on Angular Domain Imaging systems.

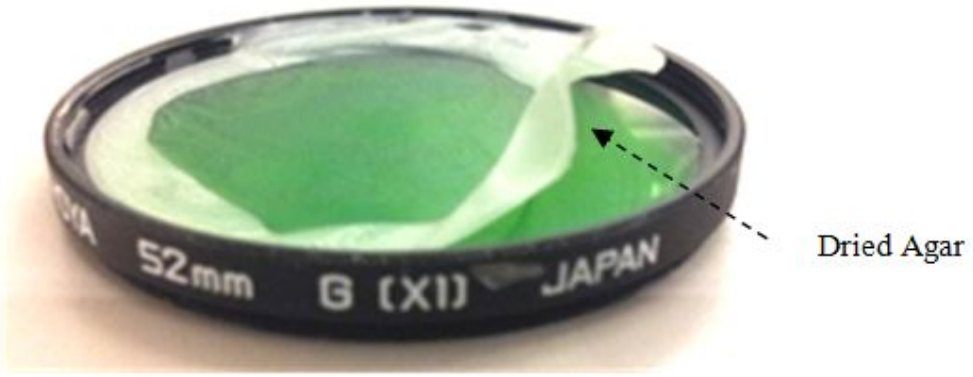

Figure 3-2: Completely Dried Intralipid Infused Agar after 3 days

Previously we showed that infusing agar with calibrated intralipid solution creates a homogenous solid scattering phantom. However, although it provides another dimension on phantom structures, it suffers another problem from other environmental impacts such as temperature and humidity. As temperature increases, the agar phantom slightly melts and slips out from the container. This means it can only be held vertically in a very short period of time which is not favorable for most optical systems. This is another major problem as we only have a short usable period to manipulate the phantom in the position we desired before it melts unless we have a well temperature controlled environment.

3.4 Encapsulated Intralipid Infused Agar

As mentioned, the existing agar phantom is sensitive to temperature and suffers from rapid drying after three days. We need to create a new technique to further extend the lifetime and usability of the scattering phantom for our ADI system. There are few requirements that we need to meet for the new phantoms.

- It has to isolate the scattering agar phantom from external environments, such as temperature and humidity.
- It has to maintain the optical characteristics of intralipid, i.e. anisotropy factor and scattering coefficient have to be remained the same for extended periods.
- It can be easily orientate in any position without changing shape.

Since the agar has a short lifetime, we tried different approaches to extend the lifetime of it. For example, we mixed intralipid solution into a clear plastic to form a scattering solid. Unfortunately, the oil contents in the intralipid separate from the plastic and the scattering plastic does not have a homogenous scattering characteristics. In tissue research, the uniformity of scattering is necessary to replicate a soft scattering tissue with no internal structures. The lack of this uniformity in a phantom creates a false positive to the system for detecting the structures within the sample. Besides mixing the solution into the plastic, we also experimented with the concepts of sealing the liquid intralipid inside a hollow plastic. This does not come out as expected. As the clear plastic (unsaturated polymer) is originally in a liquid form, when sealing the intralipid, the liquid plastic unintentionally mixed with the scattering liquid which makes this method is not preferable.

Our solution for creating a solid, stable, long lifetime scattering phantom is using a clear polymer to encapsulate and seal the solid intralipid-infused agar. We used a type of clear casting plastic resin (unsaturated polyester resin) as the clear polymer. The reason why we use this material is that first the polymer can serve as a barrier between the agar phantom and the external environment. Second it can manipulate like any other optical components, e.g. lens, prism, which has constant optical properties with refractive index ≈ 1.52. Thirdly, it has no/very-low thermal absorptivity in from UV (400nm) to NIR (900nm) wavelength (17). The characteristics make the unsaturated polyester resin is a potential candidate for this usage.

Furthermore, when creating this encapsulated intralipid infused agar, we also can combine different layers of other material based on experimental needs. For example, we can create a solid scattering phantom with:

- Fluorescence material layer
- Medium with different optical transmittance, e.g. 100%, 75%, etc
- Resolution measurement targets
- Medium with different spectrum absorption/scattering
- Multiple layers of scattering in specific locations
- and the combinations of above, e.g. a single fluorescence scattering layer

With these abilities, we are able to fabricate a more complex structure which serves as a better representation of biological tissue. In this chapter, we will be demonstrating a creation of a solid scattering phantom with 100% absorption resolution targets and autofluorescence layer. This structure is to mimic the deteriorated collagen fiber in skin tissue as the collagen fiber fluoresces while the deteriorated ones are not. This phenomenon can be used as a potential cancer screening tool for early stage of skin cancer detection.

3.5 Fabricating Encapsulated Intralipid Infused Agar for Fluorescence

In this section, we describe the creation of a test phantom mimicking skin, i.e. a fluorescent layer with dark patterns covered by a scattering medium. The creation of this new solid phantom is a multistep processes. Figure 3-3 outlines the steps in our methodology. First we create a bottom layer with outer rim with clear polymer (figure 3-3(i)). This serves as a container for latter layers to stay within the plastic. Next, we embedded a fluorescence layer by using a fluorescence plastic slide (FTIC/GFP) (18) for autofluorescence layer which mimics the collagen fiber's fluorescence behavior (figure 3-3(ii)). Then, a patterned 100% light absorption resolution target with 200μm, 300μm, and 400μm lines-and-space is placed on top of the fluorescence layer (figure 3-3(iii)). Afterwards, in figure 3-3(iv), the previously described intralipid infused agar mixture which we discussed about in section 3.3 is poured into the plastic structure. After 24 hours, when the agar mixture has set completely, we seal the scattering phantom with the unsaturated polyester resin as in figure 3-3(v). This layer and the out rim of the plastic serve as a barrier for the scattering phantom and external environment which increases the useable lifetime of the sample significantly. Finally (figure 3-3(vi)),

chemical polish from Meguiar's is used to increase the transparency of the plastic for better imaging results. Note that during this fabrication, extra care is required to avoid air bubbles or contamination trapped in the sample which inherently destroys the scattering phantom. Figure 3-4(a) shows the side view of this new solid phantom. Different layers of this phantom can be distinguished. The fluorescence layer beneath the intralipid agar layer which sealed completely by the clear plastic. Figure 3-4(b) shows the top view of it. Due to the scattering of the intralipid agar layer, we are not able to see the fluorescence and the resolution target. But when we look it from the bottom (figure 3-4(c)), the resolution measurement targets and the fluorescence can be easily seen.

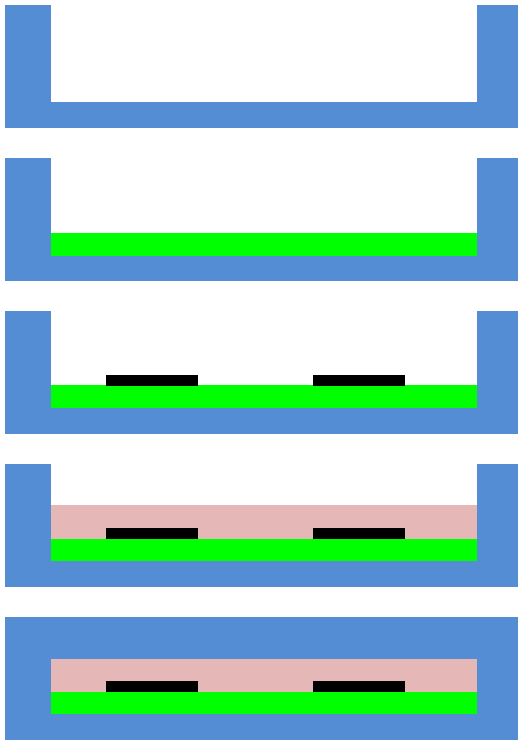

i. A bottom plastic layer with outer rim is casted.

ii. Next, embed the fluorescence layer.

iii. Afterwards, resolution target is placed on top of the fluorescence layer.

iv. Pour in the intralipid and agar mixture.

v. Seal the structure with plastic layer.

vi. Polish the solid structures with chemical to increase transparency.

Figure 3-3: Procedures on creating solid scattering structure

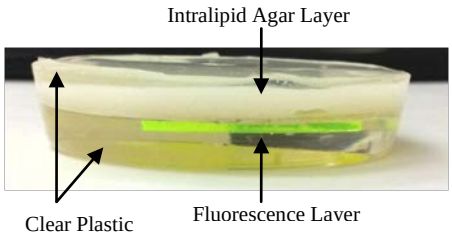

(a)

(b)

(c)

Figure 3-4: View of the Actual Solid Scattering Phantom (a) Side view (b) Top view (c) Bottom view

3.6 Scattering Ratio and Scattering Coefficient Measurements

In order to verify the stability of the solid, long lifetime scattering phantom creation, we need to measure the scattering ratio (SR) and the reduced scattering coefficient (μ_s') of the sample over a long period. We used 2 different laser sources and 3 different scattering samples with different concentration and thickness for measurements. These provide us 6 different measurements which can be used to verify the spectral behavior of the phantom and possibility of calibrating the scattering via concentration and thickness. The laser sources used in the experiment are HeNe (633nm) and Nd:YAG 2nd Harmonic (532nm) laser. The experimental setup (see figure 3-5) is done by placing the scattering phantom in between 2 apertures and the power meter is positioned 15cm away from the sample. This is to ensure only the ballistic photons enter the power meter. Measurements are taken over a course of 150 days at several times which provide us sufficient data points for long term interpolation of the scattering behavior about the encapsulated scattering phantoms. First we measured the sample every few days and after a month, a measurement is recorded a longer intervals for 150 days currently. As mentioned, we used 3 different scattering samples for the measurements.

These samples (figure 3-6) have thickness of 4mm, 6mm, and 8mm with 3 different concentrations. The differences in concentration and thickness is to ensure that this type of phantom fabrication technique can support multiple thickness of scattering structures. Noted that for each sample, we circled a target area with black tape. This is to ensure we will have a consistent measurement throughout the whole period of time. This is crucial to our analysis because we want to guarantee any changes in the agar layer could be easily identified such as thickness, color, air bubbles, etc.

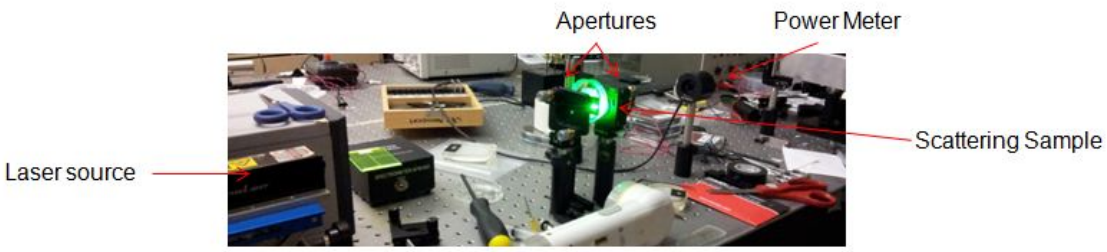

Figure 3-5: Scattering Ratio and Scattering Coefficient Measurement Experimental Setup

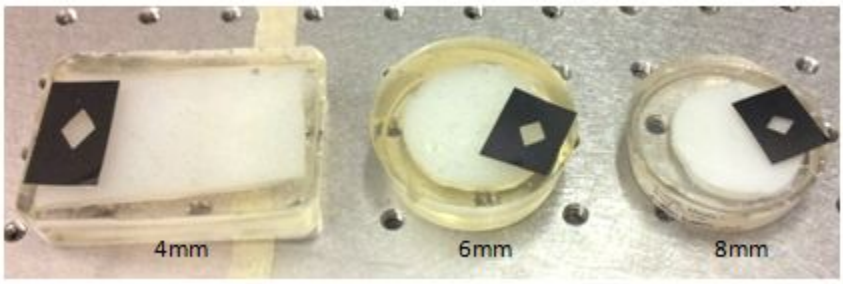

Figure 3-6: Encapsulated Intralipid Infused Agar Scattering Sample at different thickness

The scattering ratio (SR) and scattering coefficient (μ_s') is calculated based on the formulae 1 and 6 which are discussed in chapter 1. Since we are hoping to create a stable, solid, long lifetime scattering medium for ADI imaging, we have to make sure that the optical properties of the scattering phantom remains the same for at least few months. Therefore, we expect the SR and μ_s should have a zero slope theoretically in order to achieve the requirement.

3.7 Stability Results on Encapsulated Intralipid-Agar Phantoms

Using the setup in figure 3-5 and the theories behind the measurement in previous chapter, we measured our 3 sample's scattering coefficient. Figure 3-7 and 3-8 show the SR and μ_s' measurement with different scattering thickness and concentration.

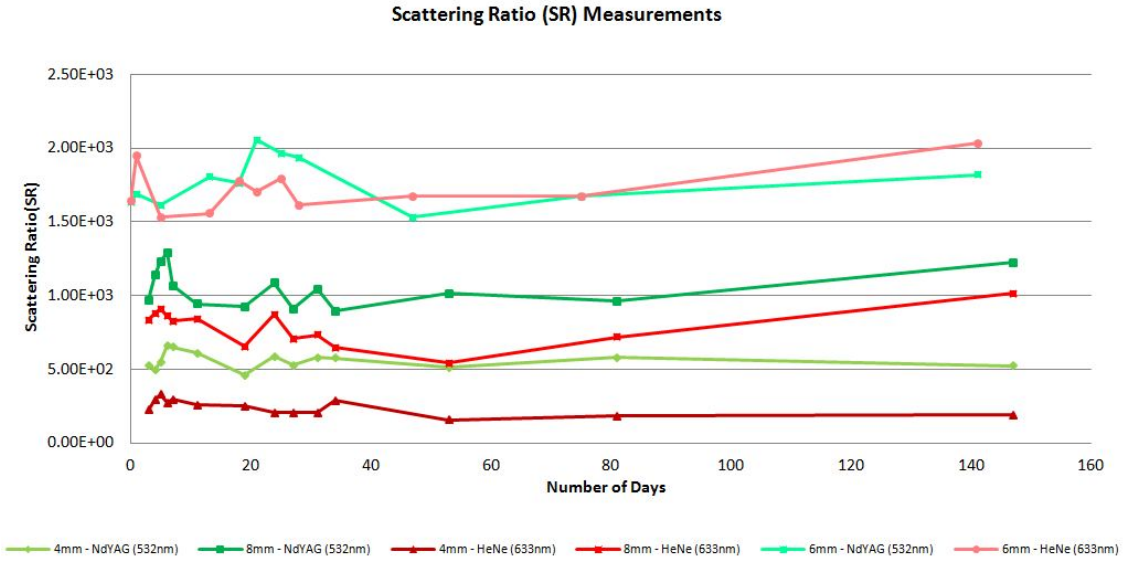

Figure 3-7: Scattering Ratio measurement with different scattering thickness and wavelength

From the measurements, we can see that the overall shape of the curve remains a relative flat line except at the first 20 days' measurements. This initial fluctuation is due to the fact that we were calibrating our measurement system setup. Although it appears to have an unstable measurement at first, the SR measurement value remains in a relative close range with respect to its scattering thickness (within 15%). When we look at the result for the μ_s', the fluctuation pattern reduces due to the Beer-Lambert law where the scattering coefficient is in the logarithmic term. This shows a promising result which we can apply error analysis to further verify our effectiveness of the measurements.

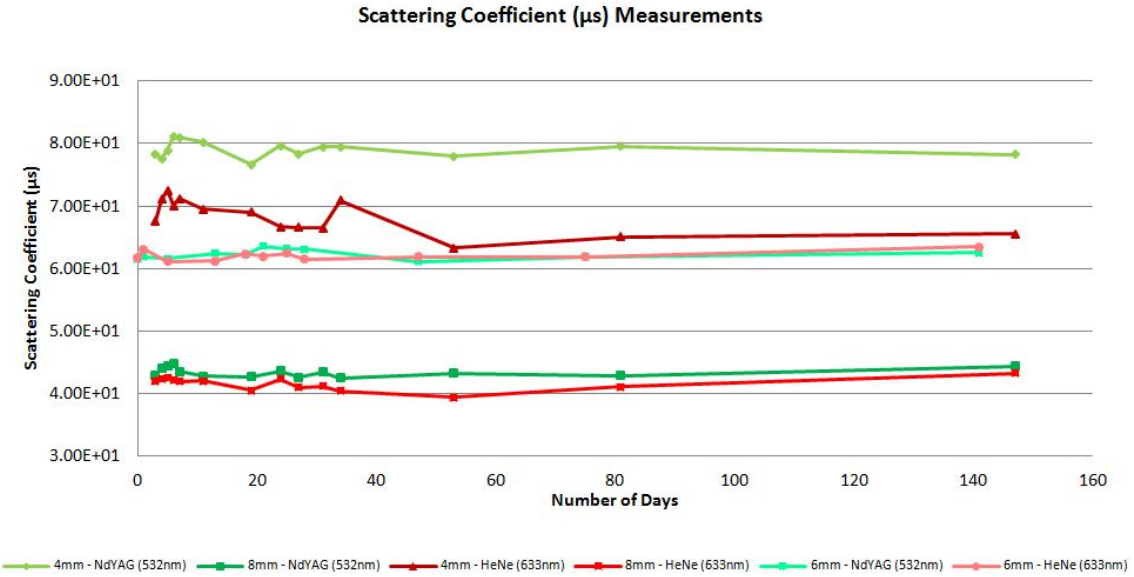

Figure 3-8: Scattering Coefficient measurement with different scattering thickness and wavelength

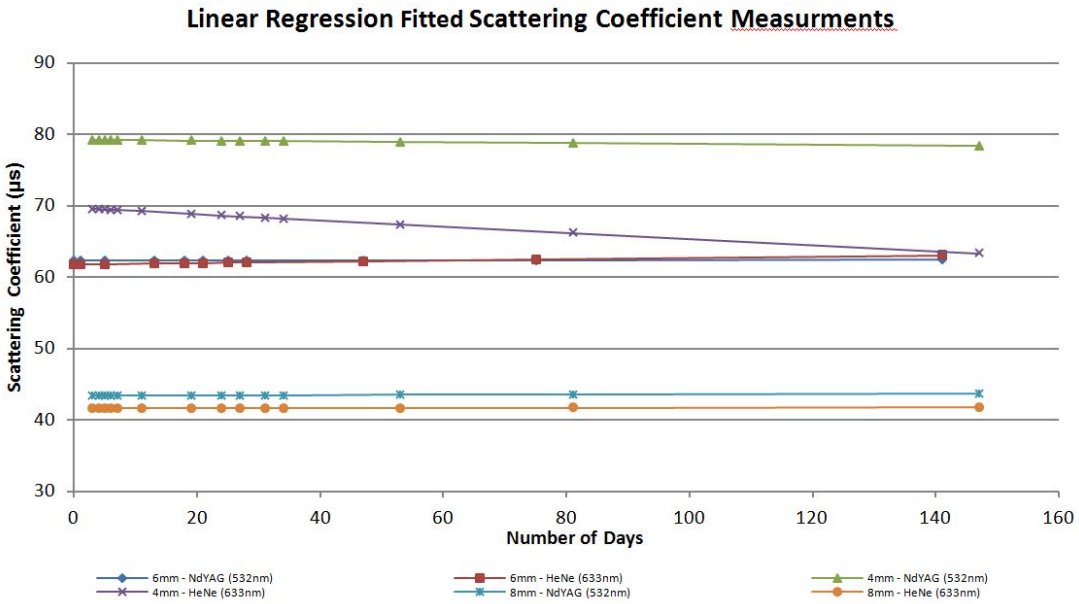

Figure 3-9: Linear Regression Fitted Scattering Coefficient measurement with different scattering thickness and wavelength

After we applied linear regression fitting (with μ_s' = B*days + A) to the reduced scattering coefficient measurement in figure 3-9, it shows that all the measurements basically maintain a horizontal profile. Table 3-1 summarizes the slopes of the fitted measurements and the standard error. From the table, it clearly shows that all the measurements show a slope of less than 0.01 (cm^{-1}/day). Looking at the ratio between slope (B) and intercept (A), i.e. B/A, all measurements showed that the slope of the degradation of the scattering medium is less than 0.05% per day. Using the t Stat for B and P-value from the table, this strongly support the linear fitting as most of the fit has roughly 70%-90% chance showing that the line is a horizontal/zero slope fitted. Based on the measurements over 150 days, the results strongly suggest that our scattering phantom can maintain a zero slope of scattering characteristics within the measurement error changes statistically over a year long period. Also, comparing the scattering coefficient of the same sample with different wavelength, the encapsulated intralipid infused agar maintains the optical property that with shorter wavelength, the scattering increases. This behavior happens in all 3 different thickness samples' measurement which supports this analysis.

Table 3-1: Linear Fitted μ_s measurements

Scattering Thickness	Laser Wavelength	Intercept (A) (cm^{-1})	Slope (B) (cm^{-1}/day)	B/A	Standard Error on B	t Stat for B	P-value
4mm	NdYAG (532nm)	79.23	-0.005	-6.31×10^{-5}	0.009	-0.624	0.543
	HeNe (633nm)	69.67	-0.04	-5.74×10^{-4}	0.015	-2.75	0.0174
6mm	NdYAG (532nm)	62.26	0.0009	1.45×10^{-5}	0.006	0.153	0.88
	HeNe (633nm)	61.79	0.009	1.45×10^{-4}	0.005	1.828	0.10
8mm	NdYAG (532nm)	43.37	0.002	4.611×10^{-5}	0.005	0.367	0.719
	HeNe (633nm)	41.56	0.001	2.41×10^{-5}	0.007	0.222	0.827

This concludes that our encapsulated intralipid infused agar has significantly increased the lifetime of the traditional intralipid infused agar by at least 49 times to more than 150 days. After we have a confident result with this stabilized scattering phantom, we investigate the feasibility of using this scattering phantom for Angular Domain Imaging. Even though we have a successful result on this new created phantoms, extra caution during the fabrication is recommended. For example, any improper sealing of the phantom, i.e. a tiny portion of the agar is exposed to air, the intralipid-agar layer in the final phantom will shrink within days no matter how small the hole is. Second, air bubbles generated due to the exothermic reaction of the unsaturated polyester resin, it is preferred to vacuum the liquid plastic to minimize the air bubbles before pouring. These problems appeared in some of the first test samples until the correct sealing methods were developed.

3.8 Chapter Conclusion

In this experiment, we successfully created a stable, solid, long lifetime scattering tissue phantom which can be used towards different types of imaging system. The scattering tissue phantom is created by encapsulating intralipid infused agar into a clear unsaturated polyester resin which isolates the scattering agar from the external environments. By securely sealed the intralipid infused agar in the polymer, we are able to manipulate this solid tissue phantom is any orientation required by the imaging system. Furthermore, this fabrication technique allows us to create a complex, multilayer human soft tissue phantom with different absorption and scattering levels, fluorescence properties, imaging targets transparency level, and spectrum absorption. Hence, we

have a better representation on mimicking human soft tissue which maintains its optical properties for over 10 months, an increase of at least 49 times in duration.

In the next chapter, we will discuss Monte Carlo Simulation on ADI which is used to assist on designing the actual 2D-collimating matrix ADI filters for future experiments. Also, the simulation will study the best acceptance angle to be used for shallow depth fluorescence ADI. Furthermore, how the difference in fluorescence behavior, e.g. natural fluorescence and injected fluorophore in ADI system.

Chapter 4: Monte Carlo Simulation

When designing a new optical component, it is beneficial to understand a photon's behavior in targeted scenarios via simulations. Since photons have random behaviors in scattering medium, a simulation which could generate a large number of random photon interactions throughout the targeted scenario is desired, i.e. a Monte Carlo Simulation. Monte Carlo methods simulate by scattering photons using a statistically large random numbers set with the same probability distribution (distance, angles) as the modeled event. With a sufficient numbers of photons, the probability distribution would match that of the scattering media.

In this thesis work, a Monte Carlo software package, called the Photon Transport Simulator (PTS), developed by Nick Pfeiffer at Simon Fraser University as part of his Ph.D. research work. PTS allows its user to simulate arbitrarily complex geometries in absorbing and scattering mediums, and optical elements like lenses or collimators. Photons move along their paths depending on the properties of the scattering medium. The simulation and the components setup is input via a text-based script. This script contains the positions of all individual components in the simulation, for example: the fluorescence emission behavior (emission angles, wavelength, density), scattering medium (scattering and absorption coefficient, anisotropy factor), optical components (lens with user defined focal length, refractive index, pinhole), multiple imaging planes in any user defined locations. With this high customization in the simulation program, we can virtually design any optical scenario via the program. This significantly minimizes the cost used in the actual optical system design or fabrication. Although this program is beneficial to optical system design, there is a major problem. In order to achieve a statistically valid distribution, a significant number of photons is required. Then simulation results are created by the count of photons pass through a capture plane which forms a 2D intensity diagram.

4.1 Fluorescence in Monte Carlo Simulation

As discussed in chapter 2, fluorescence is the emission of light of a longer wavelength after absorbing the light source at a different wavelength as showed in figure 2-2. This shift in the fluorescence excitation and emission spectra is referred to as the Stokes Shift. By studying the autofluorescence cells in tissue over time, abnormal or cancerous behaviors can be detected and observed. Fluorophores can be naturally found in tissue

or artificially inserted. Collagen is a commonly found fluorophores located approximately 1mm underneath the epidermis with an excitation spectrum of 340-470nm and an emission spectrum of 420-540nm. On the other hand, fluorescence chemical such as R6G which used majorly in fluorescence research, with an excitation spectrum at 533nm and an emission spectrum between 555-585nm, can be inserted into samples artificially. (19)

With these two targeted characteristics of fluorescence, we created two simulation scenarios of fluorescing situations are constructed in the Monte Carlo program: (1) emissions from point sources at regular intervals to emulate the artificially inserted fluorophores (in figure 4-1(a)), and (2) emission from a uniform source with non emitting areas to model the autofluorescence of collagen in tissues (in figure 4-1(b)). For the point source emission simulation, six point photon sources at 100 μm intervals each emitting 5 million photons (30 millions in total) (in figure 4-1(a)) are placed behind a scattering medium with thicknesses ranging from 1mm to 2mm. For the uniform emission simulations in figure 4-1(b), a uniformly lit background emitting with 60 million photons is placed beneath the same scattering medium.

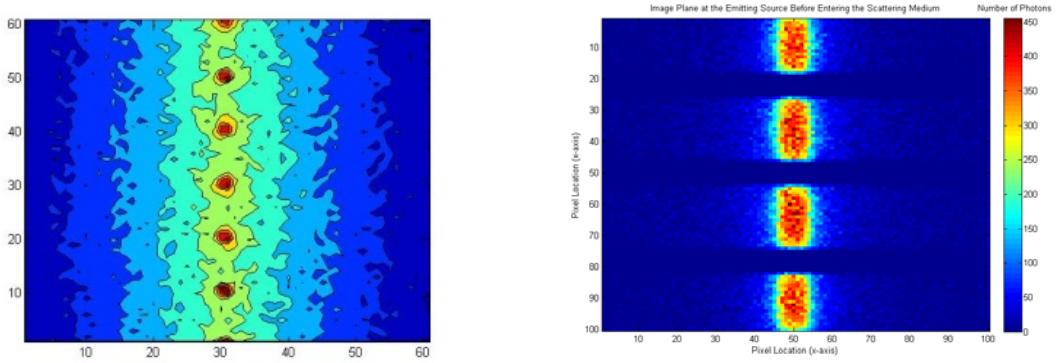

(a) **(b)**

Figure 4-1: Contour maps of Fluorescence Emission
(a) Point Source (b) Plane Source with absorbing lines

4.2 Angular Domain Imaging in Monte Carlo Simulation

Previous experiments on ADI have been focused on transillumination with samples up to 5cm in thickness (4) (20) (21). However, in the application for fluorescence imaging, ADI is targeted towards shallow structures, such as collagen cells, which are usually embedded close (~1 - 2 mm) to the surface of skin. Due to this small thickness and thus more modest scattering; the acceptance angles of the ADI filters can be adjusted to

larger angles. However, other criteria, such as resolution, have to be considered for this adjustment. In order to determine the optimal acceptance angle for both sufficiently rejecting scattering photons while maintaining an acceptable resolution, a Monte-Carlo simulation is used here to simulate ADI with shallow depth of tissues.

A 2D collimating array, which is a new type of angular filters in ADI, with different aspect ratios is placed immediately after the scattering medium with the collimating holes set at 25μm radius on 100μm centers and various lengths from 250μm to 1000μm. An additional test with a 50mm lens placed at twice the lens' focal distance to model the image sensor setup needed to capture an image in real life. The scattering medium has a scattering coefficient of 200cm^{-1}, a g factor of 0.85, an index of refraction of 1.33, and various thicknesses which is the typical value for skin covering a collagen layer . To mimic the damaged collagen, simulation scenarios of the fluorescing situation are constructed in the Monte Carlo program consisting of emissions from a uniform source to model the naturally occurred fluorophores with non emitting damaged areas. As shown in figure 4-1(b), the absorbing line is the damaged collagen which does not fluoresces.

4.3 Monte Carlo Simulation Results

As discussed previously, we want to simulate a uniform fluorescence point source/layer below 1-2mm of scattering material which is filtered by a 2D collimating array with different aspect ratio and position. First we will analyze the point source fluorescence which served as artificial injected fluorophores beneath a scattering layer.

4.3.1 Monte Carlo Simulation Results - Point Source Emissions

In general, using a point source emission for the simulation is to emulate the optical behavior when performing ADI with artificial fluorophores. This technique provides us information about the optical behavior of tissue by measuring the output intensity in various spot within a tissue which assists us to identify potential structural absorber within the tissue.

The thicknesses for modeling the biological tissue are 1mm, 1.5mm, and 2mm. This range of thickness corresponds to the location of collagen, a natural fluorophores, which is typically approximately 1mm underneath the epidermis (5). The reason for selecting

these thicknesses is that typical depth required for physicians to identify irregular tissues, such as tumors, are mostly lying on the top layers of the tissues. Furthermore, we will try to discover the imaging limitation with current proposed ADI technique. In previous research (4) (21) (22) (20) (23), we demonstrated that we are able to use the collimator holes arrays to filter out scattered photons and retrieve the photon sources location at various tissue thicknesses. Figure 4-2(a)-(d) shows us the simulation results with different optical filters, note that the figures have the same intensity across.

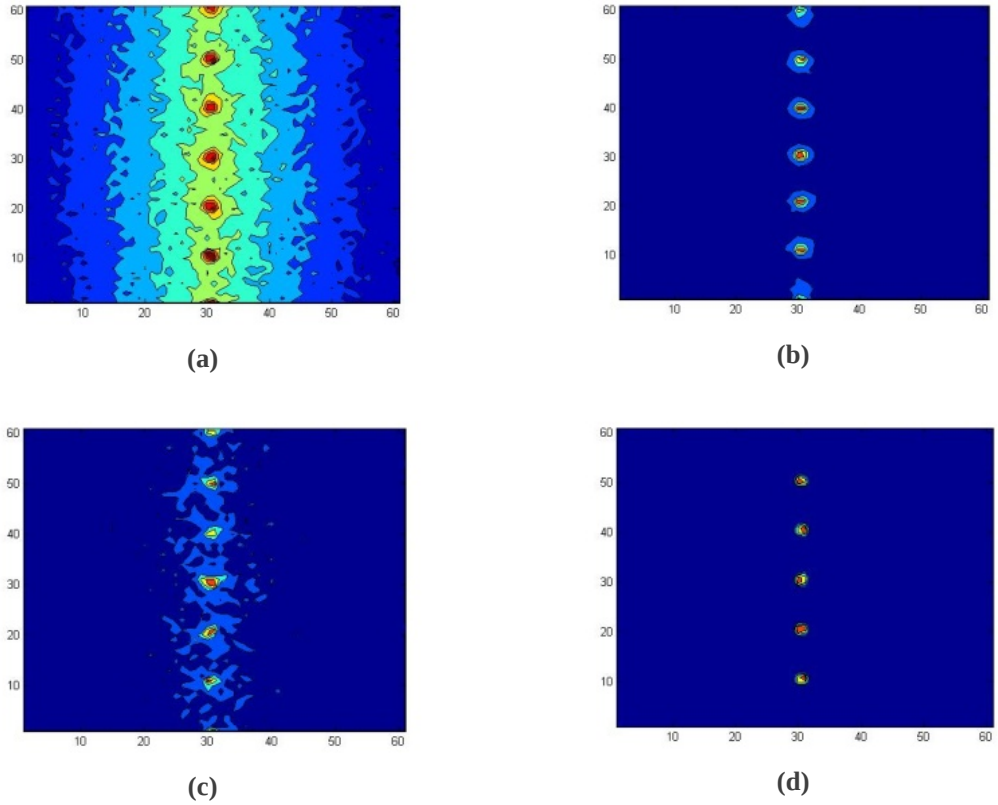

Figure 4-2: Contour maps of simulation results with scattering thickness of 2mm (a) at scattering medium surface (b) simple 50mm converging lens (c) SFF with acceptance angle of 2.5° (d) 2D collimating array with aspect ratio of 10:1

Figure 4-2(a) shows the surface distribution of photons which travel from point source fluorescence to the 2mm thick scattering medium. Note that, although it is a point source, photons are emitting uniformly in all directions which creates a line point sources where photons propagating outward from the initial emission locations. This aligns with the actual fluorescence behavior in scattering tissue. Figure 4-2(b) is a simple camera setup which consists a +50mm converging lens placed at 2 focal length from the scattering surface. We can see that this simple camera setup is able to capture the

photons from their origin which are the positions of point source. This represents what would be seen by camera imagers currently used in the literature. Although it gives acceptable result, the result also shows a small spread of photons around the point source location. Using a SpatioFrequency Filter as we discussed in chapter 2 with an acceptance angle of 2.5°, it does not produce a high quality image as in figure 4-2(c). This is because the aperture used in the SFF blocks out a larger number of photons than with the regular camera setup. Hence, the overall intensity of the photons reduces. In order to match the quality of the regular camera image, we could increase the acceptance angle which it allows more photons pass through. On the other hand, the scattered photons filtration power would be reduced.

At last, figure 4-2(d) is using the new designed 2D collimating array with aspect ratio of 10:1 ($\theta_a \approx 5.72°$) produces the best image in the group. This shows that the new design able to pick up the fluorescence photons from a point source after a shallow depth of scattering medium.

Next, we want to simulate the effects of misalignment of the 2D collimating array. This allows us to study the possible constraint when we are not able to perfectly align our collimator on the artificial fluorophores in real life situation. Figure 4-3 shows the angular domain filtered results where the collimator holes arrays are placed directly on top of the scattering surface first aligned with the source (figure 4-3(a)) with the collimator is shifted: 25μm to the right (figure 4-3(b)), 25μm to the left (figure 4-3(c)), and 50μm to the right (figure 4-3(d)). These results show that we are able to image the point sources clearly with the collimator holes array. Although the number of photons passing through the shifted collimator holes is reduced from 544 in figure 4-3(a) to 154 in figure 4-3(c), the overall image quality remains constant as the high intensity point indicates the locations of the point sources. Combining the point source which placed at a known position and the collimator array, we can use the point source as our major alignment indictor for the imaging autofluorescence layer of the tissue which happens to have a lower intensity. This minimize the alignment error when imaging the tissue.

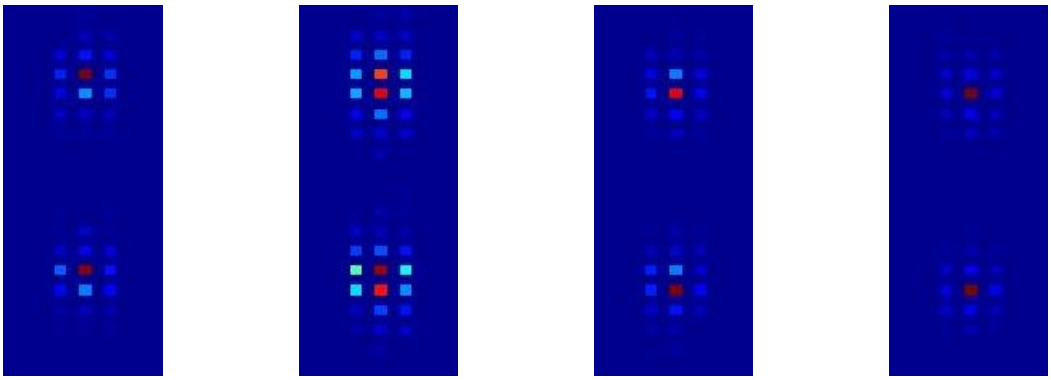

(a) (b) (c) (d)

Figure 4-3: Contour maps of collimator at various positions from the point sources (a) aligned with the sources (b) 25μm to the right of the sources (c) 50μm to the right of the sources (d) 25μm to the right of the sources

Table 4-1: Maximum number of photons detected after collimator at various positions

Position of Point Source Relative to Collimator Holes	Maximum Number of Photons Detected	% of Photon Intensity Reduction
aligned	544	0
25 μm to the right	362	33.5
between 2 holes	154	71.7
25 μm to the left	356	34.5

Table 4-1 summarizes the difference in the maximum number of photons between photon point source positions. It shows that the reduction due to shifted sources is roughly 70% to 30%. These peak photon locations remain a respectable value for the camera sensor to pick up the signals. When placing a 3-row collimator arrays right after the scattering medium, figure 4-3 shows the center spots of the point source and the 'ring' effect around the center spot. If the fluorescence is not a true point source, the effect of this shifting will be reduced. These results suggest that with a modest aspect ratio of 10:1 with modest scattering thickness of up to 2mm, we can readily identify fluorescence point sources through tissue.

4.3.2 Monte Carlo Simulation Results - Lambertian Plane Source Emissions

Now let us consider the effect of large area fluorescence emitter masked by absorbing regions combine with ADI. We switched the point source into a uniform plane emitting surface with different widths of absorbing/non-emitting areas to simulate the situation of collagen in tissue with damaged non-fluorescing areas.

As discussed previously, Monte Carlo simulation requires tremendous amounts of photon events to generate usable result. For this simulation, 60 millions of photons were launched in each scenario, and each simulations were taken 24 hours to complete. To reduce the time for simulating a result, we shaped a Lambertian plane source with 60 millions photons in rectangular form with horizontal absorbers lying across the surface. The absorbers have an initial width of 200μm with 1mm spacing between each absorber, as show in figure 4-4(a). Then, the photons pass through a strip of 1mm or 1.5mm thick scattering medium which bounded by a light absorbing material. Figure 4-4 (b) illustrates the image plane at the surface of the 1mm thick scattering medium. It shows that we are not able to see any absorbers within the image, as the number of scattered photons dominates to the image and the boundary light absorbing material blocks out all the light outside the strip. Comparing with figure 4-4(b) and figure 4-2(a), it shows that the dark lines on a lighted region are much harder problem than the point sources scenario. As mentioned previously, collimator holes reject scattering photons with acceptance angle based on its aspect ratio. Figure 4-4 (c) has 10:1 aspect ratio with acceptance angle of 5.72º where the dark areas are detectable. Figure 4-4 (d) has 20:1 aspect ratio with acceptance angle of 2.86º. We can see that the increase of aspect ratio allows us to see the pattern of absorbers. Then, placing a 50mm converging lens to transmit the collimator array image to a detector, the quality of imaging the absorbers increases. This is as we expected because the simple camera setup further reduces the number of scattered photons as the scattered photons diverge away from the center of its original position.

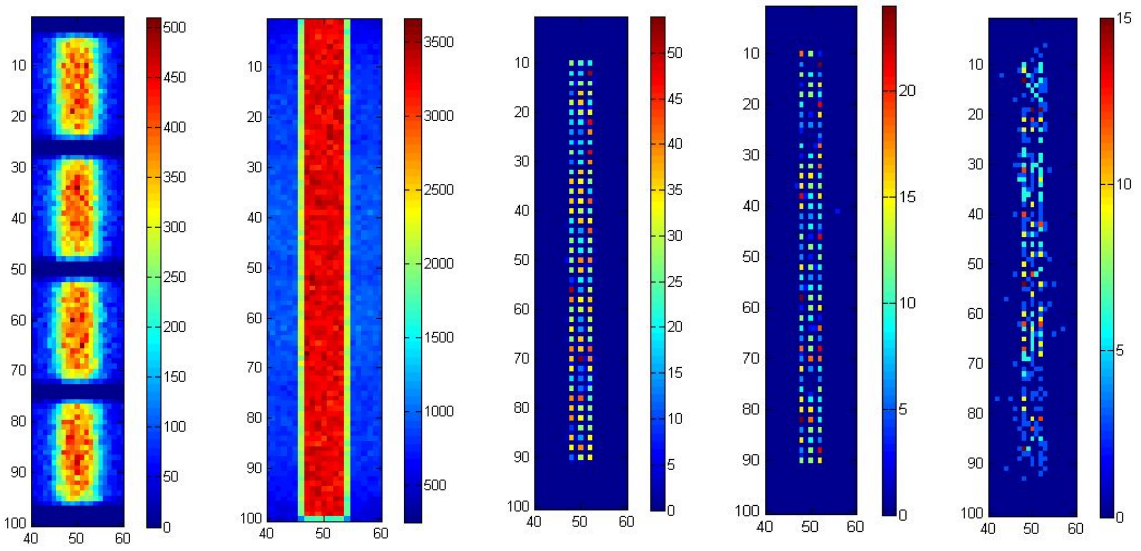

(a) **(b)** **(c)** **(d)** **(e)**

Figure 4-4: Contour maps of plane source with 1mm scattering medium
(a) Before entering the scattering medium (b) After scattering medium with 1mm thickness
(c) Collimator holes with 10:1 aspect ratio (d) Collimator holes with 20:1 aspect ratio
(e) 200mm away from the collimator holes with 50mm lens placed in between

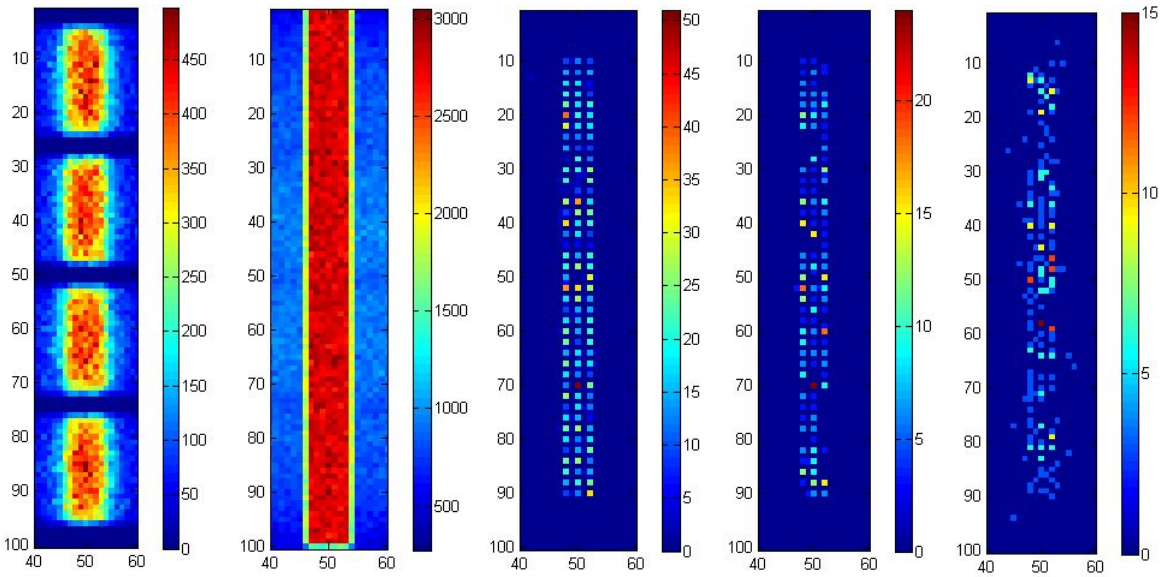

(a) **(b)** **(c)** **(d)** **(e)**

Figure 4-5: Contour maps of plane source with 1.5mm scattering medium
(a) Before entering the scattering medium (b) After scattering medium with 1mm thickness
(c) Collimator holes with 10:1 aspect ratio (d) Collimator holes with 20:1 aspect ratio
(e) 200mm away from the collimator holes with 50mm lens placed in between

As the thickness of the medium increases from 1mm to 1.5mm (figure 4-5), the proportion of ballistic photons decreases exponentially based on the Beer-Lambert law. Therefore, the number of ballistic and quasi-ballistic photons will reduce which degrades the image. Figure 4-5(c) and (d) again show the angular domain filtered images with the two acceptance angles. Comparing these images with figure 4-4(c) and (d), the intensity of the image for the high scattered medium is reduced.

In Table 4-2, we used the 1.0mm scattering thickness and 5:1 collimator holes as a baseline to compare what fraction of photons has been captured as we increase the scattering thickness and the collimator hole's aspect ratio. When we increase the medium thickness from 1.0mm to 1.5mm with 5:1 aspect ratio, 80.3% of the photons passed through. This shows that when scattering increases, the ballistics and quasi-ballistics photons decreases. When we keep the scattering at 1.0mm and change the aspect ratio from 5:1 to 20:1, only 5.7% of photons passed through. This shows with a higher the aspect ratio (smaller acceptance angle), most of the photons are being rejected.

Table 4-2: Total number of photons detected after different collimator aspect ratio and medium thickness

Medium Thickness	Collimator Holes Aspect Ratio	Total Number of Photons Detected	% of Photon Detect w.r.t. 1.0mm w/ 5:1 aspect ratio
1.0mm	5:1	23028	nil
	10:1	3750	16.3
	15:1	1959	8.5
	20:1	1323	5.7
1.5mm	5:1	18498	80.3
	10:1	2361	10.3
	15:1	1113	4.8
	20:1	681	2.9

4.4 Chapter conclusion

Before we actually fabricate our new 2D collimating array angular filter, we used Monte Carlo Simulation to help us study the theoretical performance of this filter in shallow scattering depth with fluorescence. The simulations indicate that collimating arrays with modest aspect ratios work well in detecting fluorescence in shallow depths at tissue scattering levels. When using point sources, we can detect them with depth up to 2mm, independent of location. Also, we can image the filtrated image with a simple camera setup. With uniform sources, collimator array shows that with 10:1 and 20:1 aspect ratio,

can image absorbers up to 200μm width at 1mm depth. As absorbing area increase, image resolution increases, and adding a lens to image the collimating array enhance the detection even further.

The Monte Carlo simulation results provided us a ballpark on how the actual experiment setup would be would perform. As noted a 2D collimating array with a 10:1 aspect ratio collimating holes with 100μm diameter and 200μm center-to-center spacing will be fabricated for the actual experiment.

In the next chapter, the actual 2D collimator array will be fabricated and tested with shallow scattering thickness phantom with fluorescence source. Imaging results will be presented and analyzed and how it performs compare to our simulations.

Chapter 5: 2D Collimator Array Angular Domain Imaging

In this chapter, we used the 2D Collimator Array angular filter which we discussed in section 2.2 and built using acceptance angle suggested from the results of our Monte Carlo simulations in chapter 4. The 2D collimator array is designed to be used towards a shallow scattering thickness (~1-2mm) which differs from the previous experiments where the target thickness is in centimeter range. Then, the results will be analyzed and compared with our simulation results.

5.1 Experimental Problems with Artificially Injected Point Source Fluorophores

As discussed in the previous chapter, initially we would like to study the potential of performing ADI on artificial fluorophores under thin layer of skin tissue. Our simulation has shown a promising result which indicates our new 2D collimator array could detect the injection under a 2mm thick scattering. Since we were using a fluorescence slide as our fluorescence source, we need a layer of high absorption material with a small hole in a diameter of one micron to replicate the scenario in the simulation. Unfortunately, due to the limitation of our in-house laser power drilling system, we were not able to fabricate a mask with a series of hole which roughly a micron wide on a high enough light absorption material. For example, a thin sheet of aluminum which sputtered on a glass slide only has roughly a 100:1 absorption (1% transmittance / 2 OD). This is not sufficient for our required experiments. The problem is that the emitting area is several hundred times smaller than the dark background. Hence, even at 1% transmission, the scattered light leaks over the dark area which exceeds the light from the point source. In order to create our original case, a material with at least 1000:1 absorption (0.1% transmittance / 3 Optical Density) and able to use on our laser power drilling system is required. Therefore, in future planning, we need to find such material that is suitable this usage and perform this experiment.

5.2 Plane Source Fluorescence ADI Experimental Setup

The intention of this section is to explore ADI for using in the detection of collagen fluorescence patterns beneath the scattering tissue of the skin. As we intended to use a fluorescence source for our system, a fluorescent infused plastic slide is used as our illumination source. The fluorescing material used in this experiment has an excitation spectrum centered at 415nm, and emission spectrum centered at 580nm. A LED array operating at 415nm was used to provide the excitation source to the fluorescing slide

which was placed beneath a 1mm thick surface roughened glass layer. This surface roughed glass is created by using a chemical etch to give out a frosted glass effect. The time period of the roughening process determines the scattered ratio of this glass.

Figure 5-1: Resolution Targets

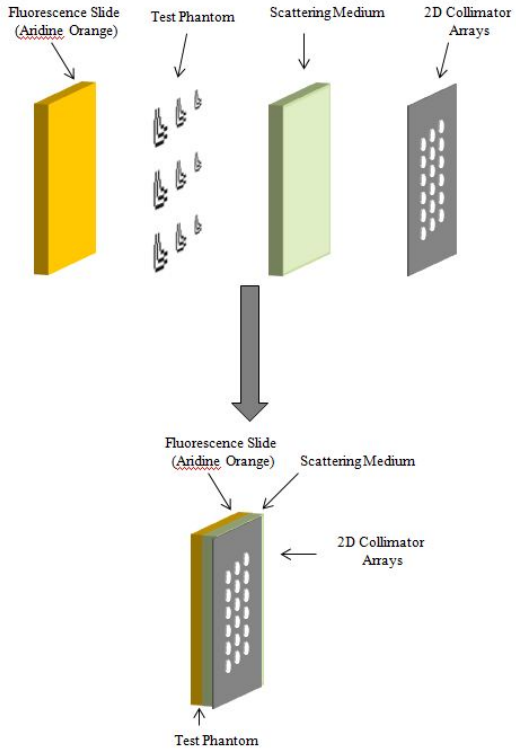

Figure 5-2: Close up view of Test Phantom

Opaque, planar resolution measuring targets with 200µm, 300µm, and 400µm lines-and-spaces were designed (figure 5-1). The reason we used such dimension as our resolution target is that these are in the range of the size accuracy needed to detect tongue tumor which does not autofluorescent while a normal tongue collagen tissue does (24) (25). Hence, this showed that Fluorescence 2D Collimating Array ADI can be applied towards different areas. This resolution target is placed in between the fluorescing slides and the roughened glass (see Figure 5-1 and 2) with no spacing in between to create the desired illumination patterns.

Next, the 2D-AFA ADI system, which was mounted on a stepping motor, consisted of the 2D collimator array, two +75mm converging lenses, and a CMOS sensor. The stepping motor was used to horizontally move the whole imaging system for a series of scans. The collimator array was placed right next to the roughened glass with minimal distance

in order for the 2D-AFA to work. After that, the first +75mm converging lens was positioned at its focal length (75mm) from the collimator and the second +75mm converging lens positioned at two times the focal length (150mm) from the collimator. Finally, the wavelength filter and the CMOS sensor were located at three times the focal length of the converging lens from the collimator (225mm) as showed in figure 5-3.

To analyze the photons pathway after they exit the 2D collimator array, we calculated the overall lens system matrix as in figure 5-4 which created a ray tracing of the optical system. First, let us look at the parallel photons. When the collimated photons ($\theta = 0°$) exit the collimator array, they travel to the first lens with their initial height. Then, the first lens converges the photons towards the focal point which is located at 150mm,. This is the second lens' position. Since all collimated photons are converging towards the focal point of the first lens which also the center point of the second lens, the second +75mm lens is virtually invisible to these photons. After the second lens, the converging photons continue their path and reach the imaging plane (figure 5-5). This creates an inverted imaging with 1x magnification. Figure 5-5 which showed 3 sample collimator holes: the center hole, the one above it, and the one below it, all photons position at the imaging plane (225mm) are inverted.

Now, let us study the photons that exit within the acceptance angle of the collimator ($\theta_a = 5.72°$). Since the photons are now travelling in a cone of light, they are not parallel/collimated. When the photons are not parallel to the optical axis, the regular ray tracing diagram (figure 5-5) does not work. Using the lens system matrix in figure 5-4, we are calculated the photon's location and its angle at 3 different planes. These planes are the first converging lens (75mm), the second converging lens (150mm), and the imaging plane (225mm). Figure 5-6 showed a ray tracing of the #10 collimator hole where its center located 1.32mm from the optical axis, but the same type of result applies to all the collimator holes' position.

Three different cases have been calculated to cover the extreme photon paths. First, the photon exits parallel to the optical axis ($\theta = 0°$). Second, the photon exits upward at half of the acceptance angle ($\theta = 2.86°$). Third, the photon exits downward at half of the acceptance angle ($\theta = -2.86°$). Analyzing the trace, we are able to see the photons diverges away from the collimator hole ($y = 1.32$mm) until they reach the first lens plane.

At this plane, all three rays are diverging at the same angle towards the optical axis with equal distance separation. This shows that the rays are collimated after the lens. When they arrive at the second lens, the parallel photon continues its path without extra alteration as the lens remains virtually invisible to this photon where it is on the optical axis. On the other hand, the two extremes are being focused towards the focal point (225mm) of the second lens which is the image plane. As a result, all three rays intercept at the image plane. Hence, a focused image is produced. By performing ray tracing using these cases, we concluded that the second lens of this optics system mainly used to focus the cone of diverging light exits the collimator where this lens is theoretically invisible to the parallel light. This lens is extremely important for capture a quality image in this imaging system as the amount of ballistic/parallel photon is significantly lesser than quasi-ballistic/diverging photons.

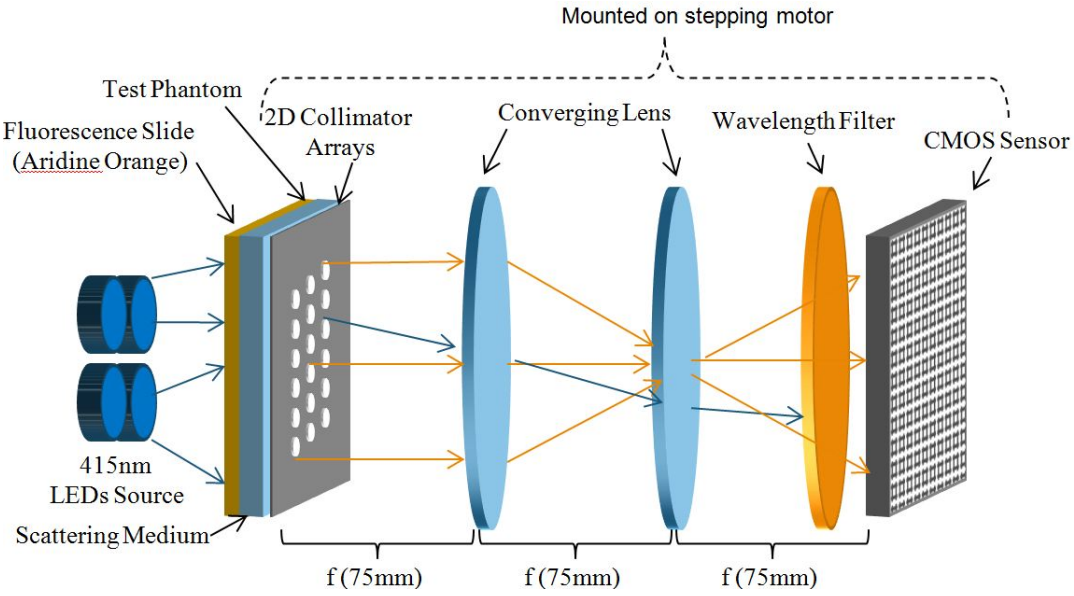

Figure 5-3: Experimental Setup with Back Excitation Illumination

$$\begin{bmatrix} H_2 \\ \tan(\theta_2) \end{bmatrix} = \begin{bmatrix} 1 & 75 \\ 0 & 1 \end{bmatrix} \begin{bmatrix} 1 & 0 \\ -1/75 & 1 \end{bmatrix} \begin{bmatrix} 1 & 75 \\ 0 & 1 \end{bmatrix} \begin{bmatrix} 1 & 0 \\ -1/75 & 1 \end{bmatrix} \begin{bmatrix} 1 & 75 \\ 0 & 1 \end{bmatrix} \begin{bmatrix} H_1 \\ \tan(\theta_1) \end{bmatrix}$$

Image Position and Angle | Image Distance (img = 75mm) | Lens 2 (f = +75mm) | Distance (d = 75mm) | Lens 1 (f = +75mm) | Object Distance (obj = 75mm) | Object Position and Angle

$$\begin{bmatrix} H_2 \\ \tan(\theta_2) \end{bmatrix} = \begin{bmatrix} -1 & 0 \\ -1/75 & -1 \end{bmatrix} \begin{bmatrix} H_1 \\ \tan(\theta_1) \end{bmatrix}$$

Image Position and Angle | System Matrix | Object Position and Angle

where :
H_1 is the photon's exit position at the collimator
θ_1 is the photon's exit angle at the collimator
(second focal length = +75mm, second principal point = -75mm)

Figure 5-4: Lens System Matrix for Ray Tracing

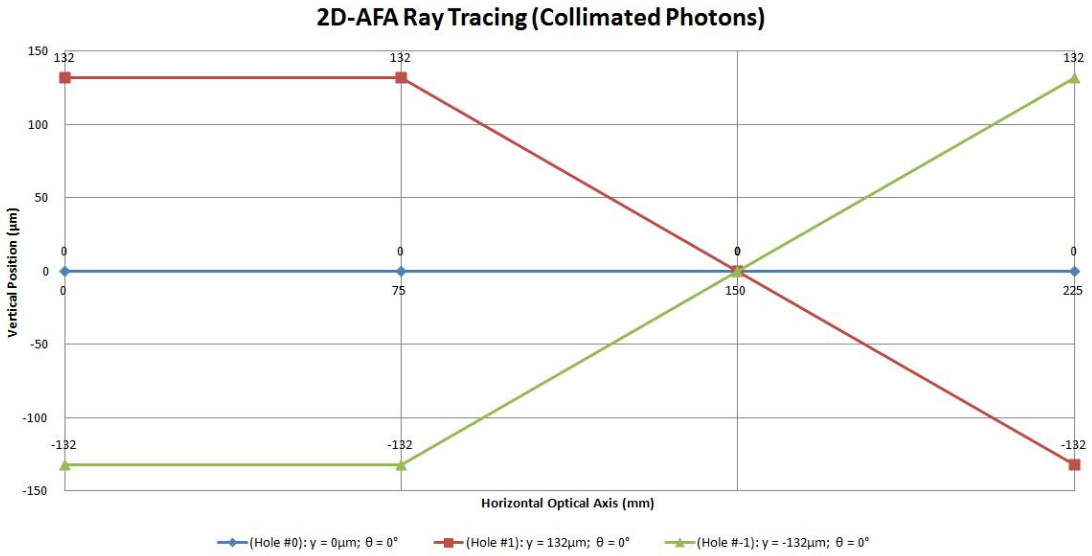

Figure 5-5: 2D-AFA Collimated Photons Ray Tracing

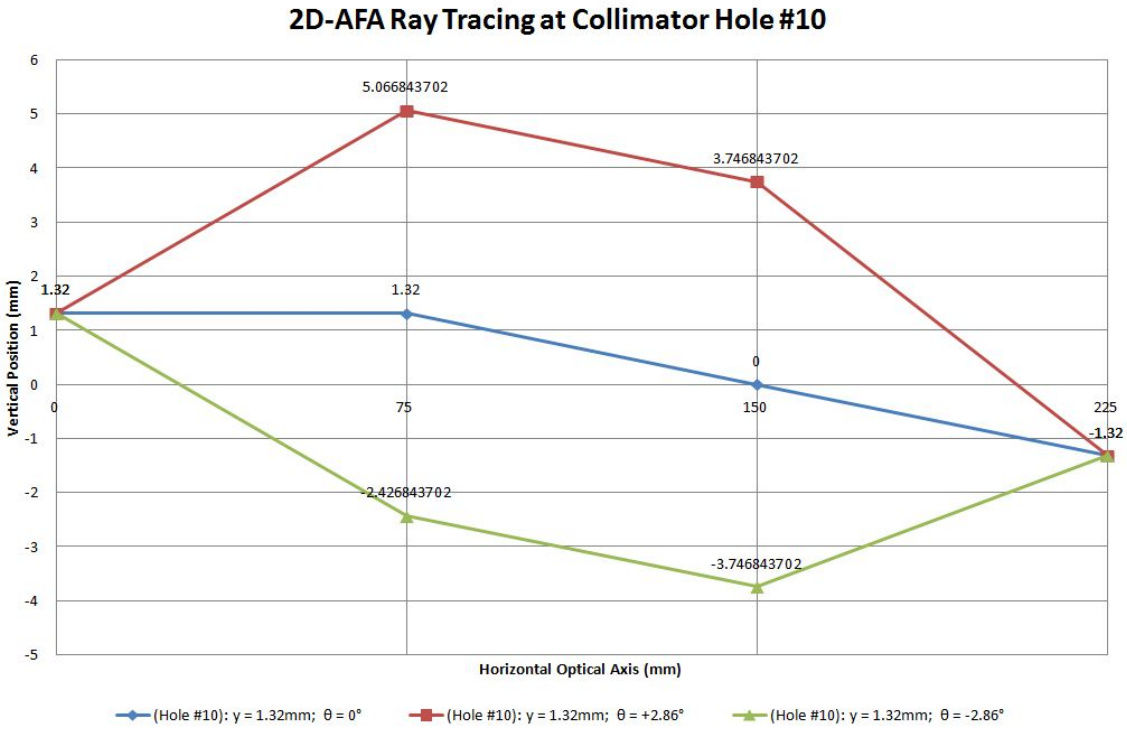

Figure 5-6: 2D-AFA Ray Tracing at Collimator Hole #10

From the simulation results, we designed our 2D collimator array to have a 10:1 aspect ratio which gives us an acceptance angle of 5.72º. The main reason we chose to fabricate our angular filters to have 10:1 aspect ratio is due to the physical properties of the material and the way of the fabrication we used. Since we are using power laser drill

system (figure 5-7) from my colleague, the minimal hole this system able to drill through this ABS plastic is roughly 100μm without damaging the nearby holes as discussed thoroughly in chapter 2. As a result, a 2D collimator array with 10:1 aspect ratio is optimal for this experiment. Although one may argue that having a higher aspect ratio, for example 20:1 (acceptance angle of 2.86º), could have a higher filtration. Hence, more scattered photons will be filtered out. But, when we look at the simulation result (figure 4-5(d)), this is not true. With a higher acceptance angle in a shallow depth situation, a large number of quasi-ballistic photons are rejected. Hence, overall image quality decreases compare to a 10:1 aspect ratio filtration (figure 4-5(c)).

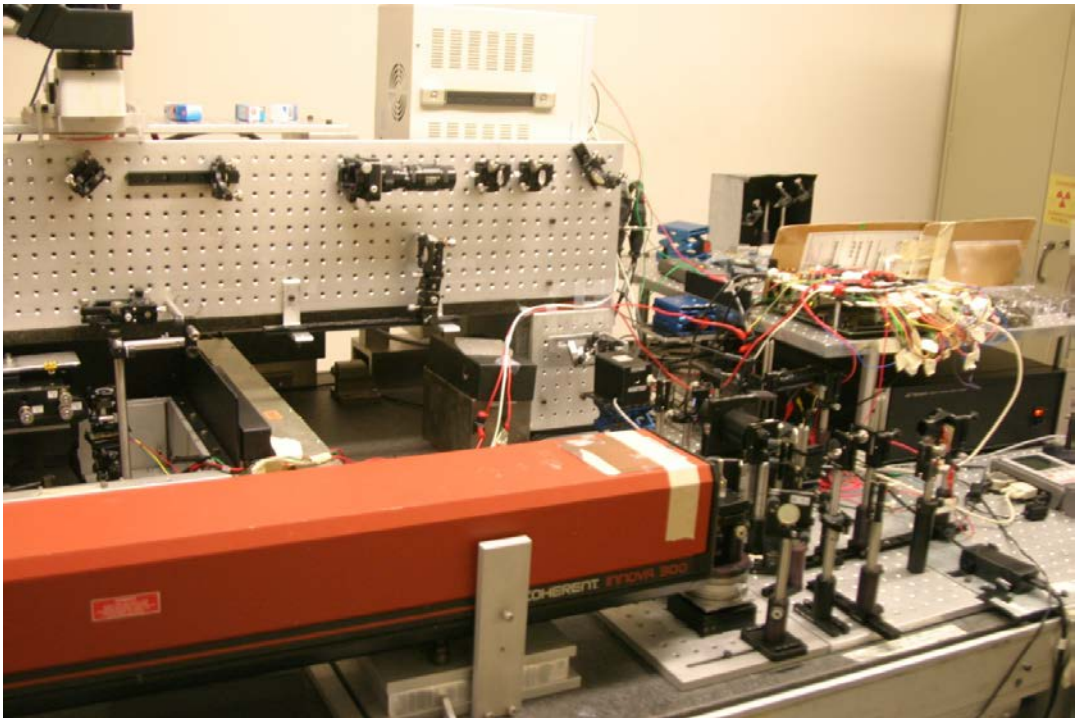

Figure 5-7: Argon Power Laser Drilling System

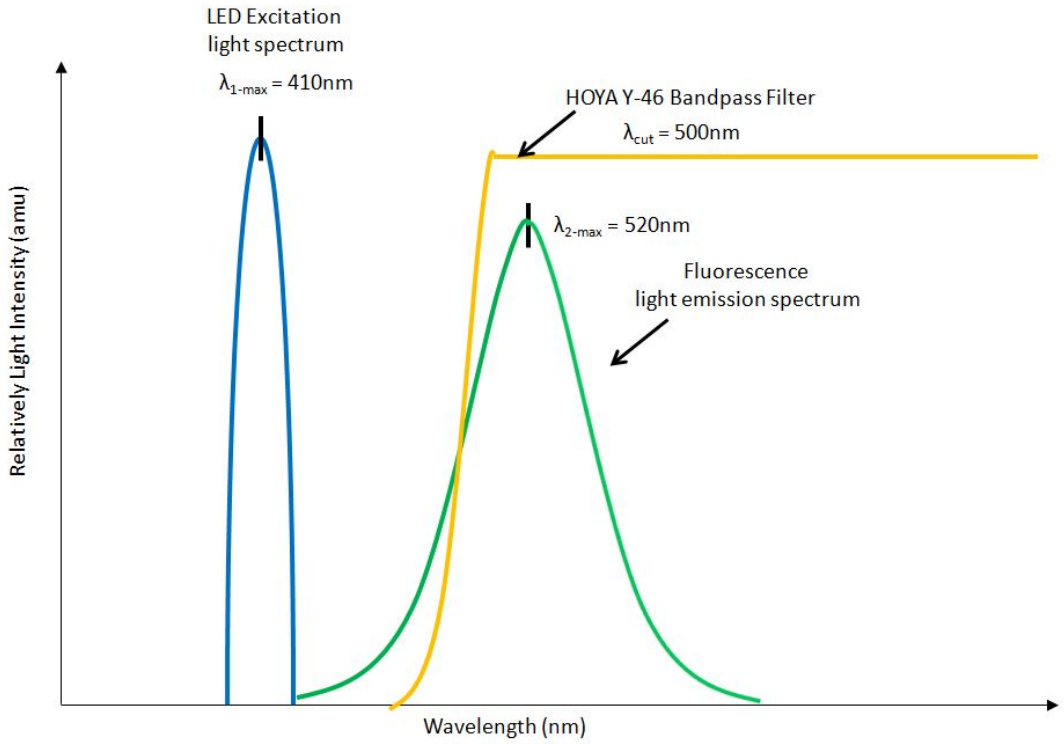

Figure 5-8: Wavelength spectrum of excitation, emission, and excitation filtration

To provide an evenly distributed excitation source, an array of 415nm LEDs was configured to have 40mW combined power output which has a nearly uniform light spread characteristics. This type of light emission produces a good model of the illumination used to create auto-fluorescence of the collagen. Filtering out the excitation at the image sensor was performed by adding a HOYA Y-46 (Yellow) colored filter in front of the image sensor. This more closely resembles the fluorescence situations in collagen, with an excitation spectrum peaked at 415nm and an emission spectrum peaked at 520nm (figure 5-8). The excitation source was positioned at either the back of the samples as shown in Figure 5-3.

The image sensor used in the experiment is a Canon EOS 10D DSLR with a CMOS imaging sensor size of 22.7mm by 15.1mm. Using a DSLR camera sensor has a several advantages over a scientific camera because of its bigger sensor area, longer exposure setting, and high ISO rating.

5.3 Fluorescence Test Phantoms

Note that the reason why we did not perform this ADI experiment with the new designed phantom which talked about in chapter 3 is that this experiment was done before the new phantom was designed. In fact, the problems encountered in these experiments encouraged us to develop the solid scattering phantom as in chapter 3. In future, we plan to perform the same experiment with the new phantom. Fluorescence slides were used as the fluorescent source in our experiments, a special thanks to Chroma for supplying these fluorescent materials to our research group. The fluorescence slides used was a yellow slide (Acridine Orange) which has an emission peaks around 580nm. In order to create the fluorescence, 10mW 415nm LEDs light source selected as the excitation source. To maximize the excitation light intensity and illumination area, 4 LEDs light sources formed a rectangular array. The fluorescence characteristic of the yellow emission fluorescence slide mimics the spectral response similar to the collagen with this setup.

Since human skin tissue thickness is roughly 1mm at the collagen layer with a scattering coefficient of 200cm^{-1}, a g factor of 0.85, an index of refraction of 1.33: this gives us a scattering ratio of ~20. This scattering ratio served as the baseline for our artificially created scattered sample. To maintain the thin tissue thickness of 1mm, a roughened surface glass with 1mm thickness is carefully fabricated to approximate SR of the biological tissue. Using a chemical etching technique, 2 scattering mediums with different SR of 3.61 (~0.5mm tissue thickness) and 328 (~2mm tissue thickness) are created. This scattering ratio covers a range of scattering medium thickness (~0.5mm to 2 mm) which allows us to study the performance of this ADI system on actual human skin tissue. And this 2D collimator array filter requires a direct contact to the scattering surface in order to have proper filtration which does not able to apply on the solid scattering phantom due to current fabrication technique.

For the 2D collimator array, a 10 x 60 arrays of collimator holes with diameter of 88µm and center-to-center spacing of 200µm on a 0.85mm thick plastic film to produce a 9.65:1 aspect ratio collimator holes. This aspect ratio is close to the desired 10:1 aspect ratio from our Monte Carlo simulation analysis as we discussed thoroughly in chapter 4.

5.4 Fluorescence ADI with 2D Collimating Array Results

As we discussed the fluorescence test phantom and the experimental setup in previous sections, we performed this shallow depth fluorescence ADI. This experiment is proposed to mimic the detection of fluorescencing collagen pattern under a 1-2mm thick skin tissue. First, we carried out a back excitation illumination source which gave a cleanest result.

5.4.1 Back Excitation Illumination Source

Since back excitation is simpler, we first perform a back excitation illumination where the 415nm LEDs are placed right behind the fluorescence slide. This removes the effect of the scattering of the excitation source before reaching the fluorescence layer (see figure 5-3). Since our 2D collimating array does not cover the whole phantom area, a series of horizontal scan performed to produce a full view image. The horizontal scan motion is executed by a T-Cube Stepper Motor Controller from Throlabs via a user program control panel where the optical components are mounted on it as in figure 5-3. After each single scan, the stepping motor moves for 100μm horizontally. Then, another scan is taken. Once we finished a complete scan, images are then stitched together via Matlab function which is written by my colleague, Polly Tsui (in section 8.4 of (26)) and me.

First, we did the experiment with the less scattered surface roughened glass with scattering ratio of 3.61 as shown in Figure 5-6, which acts like a skin tissue of 0.5mm thickness.

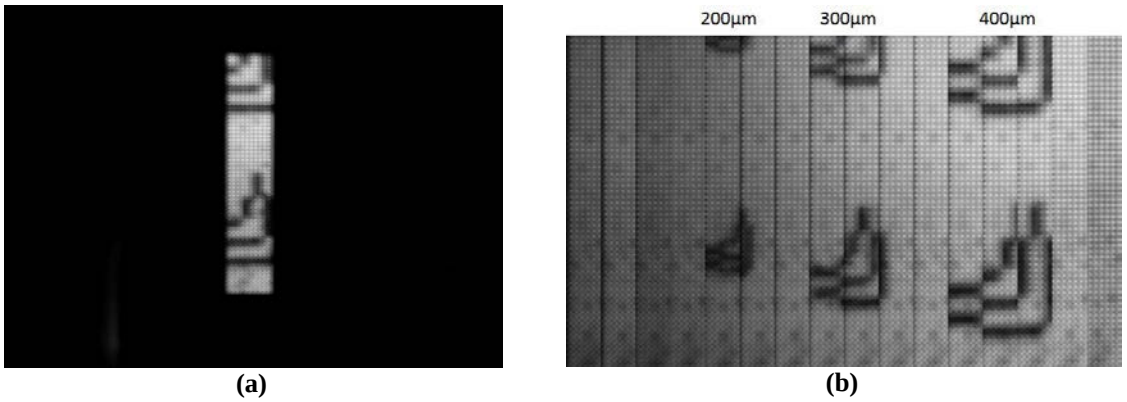

(a) **(b)**

Figure 5-9: (a) ADI scan at one position (b) a series horizontal scan stitched image with SR = 3.61

Figure 5-6(a) shows a single capture of the thin film phantom and Figure 5-6(b) showed a stitched image with a series of horizontal scan. We can see our ADI system can clearly capture the phantom structures up to 200μm which is our desired target size. To quantify the quality of the image, MTF is calculated to study the performance of the ADI system. By using formula 9, we have a $MTF_{(200\mu m)}$ = 0.27, $MTF_{(300\mu m)}$ = 0.53, $MTF_{(400\mu m)}$ = 0.65. We can see that when a larger lines-and-spaces for example with the 400μm, the MTF is 0.65. In the same scattering, but with smaller lines-and-spaces such as 200μm, the MTF drops to 0.27. Note that, in this experiment MTF is calculated by measuring the minimum and maximum light intensity of the collimator holes. The reason is that the light appears in between the holes do not accurately represent the actual light passes through one collimator holes. This could be a combination of the scattered light around a neighborhood of holes when the photons exit at angle.

Next, we changed the scattering medium to the higher scattering one with SR of 328 which acts like a 2mm of skin tissue. As the scattering ratio increased by roughly 100 times, the overall light intensity of the ADI image will be decreased significantly. Therefore, our target is to capture an image with $MTF_{(200\mu m)}$ greater than the detectable minimum (0.03).

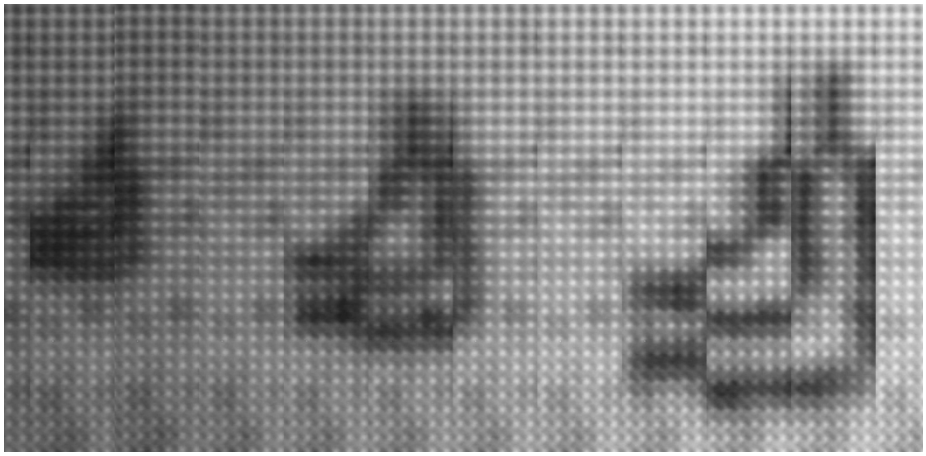

Figure 5-10: ADI with Scattering Medium at SR = 328 ($MTF_{(200\mu m)}$=0.093, $MTF_{(300\mu m)}$=0.26, $MTF_{(400\mu m)}$=0.28)

When the scattering ratio was increased by 100 times, as expected the image quality of the structures reduced significant as in Figure 5-7. Although the MTF was reduced, the smallest structure of 200μm lines/spaces remains visible. With this amount of scattering, the $MTF_{(200\mu m)}$ of the image is 0.093 ($MTF_{(300\mu m)}$=0.26, $MTF_{(400\mu m)}$=0.28). From the MTF, we know that this is near the detection limit of the image system which is 0.03. However

even with this low MTF, 200µm lines/spaces structures remain visible. The reason is that the spacing between the collimator holes provides a distinct MTF differences, hence the test phantoms remain recognizable. Also, from MTF we calculated in these 2 SR experiments, we can conclude that the MTF of optics does not affect our imaging quality. For example, when SR = 3.61 (figure 5-6(b), the 200µm target is clearly detected. When SR increased to 328, the same target is merely detected with the lack of internal details, i.e. spaces between lines. Therefore, in this system the scattering is the only factor that degrades the MTF.

Using this setup, we clearly see the ability of the ADI to image through up to a 2mm thickness scattering medium. Unfortunately, the phantom structures are not as clearly visible under high scattering environment. We suspect that the depth of focus within the system affects the imaging quality. Therefore, we will adjust the depth of focus of the system by adjusting the second lens of the simple combined lens system.

Figure 5-8(a) and (b) show the ADI image of a scattering medium with scattering ratio of 328 with different focusing points. Figure 5-8(a) shows the image is being focused at the structure while Figure 5-8(b) showed the image is being focused at the end of the collimator. At first, when the image is focused at the structures, the dark space between collimator holes diminishes because the focal point of the system is at the structures; the collimator is out focused to the system. On the other hand, when the system is focused at the collimator, the spacing between each collimator hole is clearly shown. Hence, a slightly better image quality appeared to be captured. This leads us to suspect that the image quality of the 2D collimator arrays is defined by the MTF between the holes spacing instead of the collimator holes itself. When calculating the MTF of the structures inside the picture, it clearly shows an improvement of the MTF (0.094 to 0.12 for 200µm lines/spaces) when focusing at the collimator holes. Figure 5-9 illustrates how the intensity difference between collimator holes resembles the structures. As the structure is right underneath the collimator, the light intensity is less than that of the illuminated plain scattering medium. The reason why there will be some intensity at the structure's position is that scattered light within the medium passes through the collimator holes.

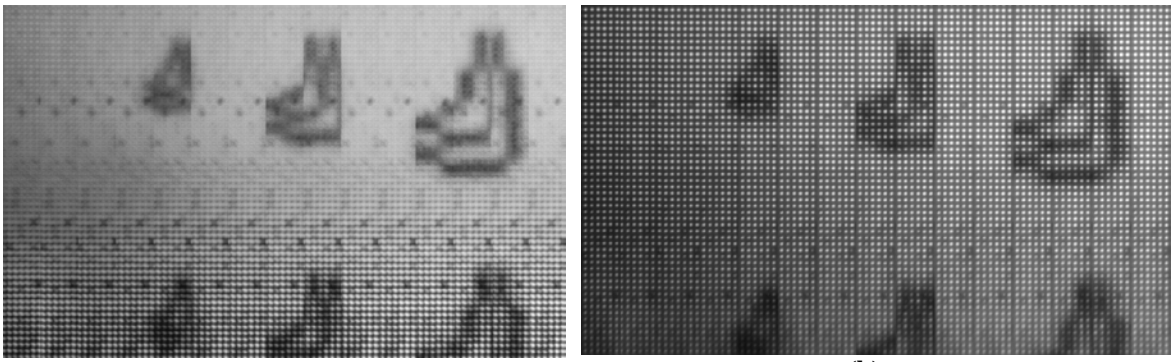

(a) **(b)**

Figure 5-11: ADI with Scattering Medium at SR = 328
(a) Focused at Structures ($MTF_{(200\mu m)}$=0.094, $MTF_{(300\mu m)}$=0.11, $MTF_{(400\mu m)}$=0.26)
(b) Focused at Collimator Arrays ($MTF_{(200\mu m)}$=0.12, $MTF_{(300\mu m)}$=0.21, $MTF_{(400\mu m)}$=0.30)

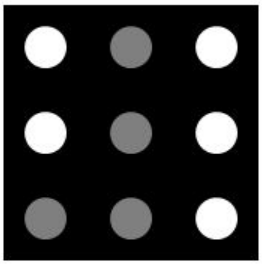

Figure 5-12: Structure appearance at collimator

When calculating the MTF for both images with the method of measuring the intensity of the collimator holes, Figure 5-8(a)'s $MTF_{(200\mu m)}$ is 0.094 and Figure 5-8(b)'s $MTF_{(200\mu m)}$ is 0.12. We can see there is a slight improvement on the MTF which possibly be we are measuring the MTF of the structures on the scattering surface in Figure 5-8(a) and measuring the MTF of the structures on the collimator in Figure 5-8(b). By changing the focal plane of the collimator, the $MTF_{(200\mu m)}$ increases 21%.This improvement of MTF suggested that structures are imaged with the 2D collimator array is best defined by the focusing on the collimator holes.

5.4.2 Front Excitation Illumination Source

While back excitation illumination is useful experimentally, for real tissue problems, we would need an excitation source that passes through the scattering skin first. With front excitation illumination, this simulates the actual fluorescence behavior where fluorphores are located under the surface of the scattering medium and illuminated from above. As we are able to image through a modest thickness of scattering medium with scattering

ratio of 328 using back illumination, we decided to conduct a front excitation illumination source for this fluorescence ADI setup (see figure 5-10) using the scattering medium with SR of 328. The reason we skipped the lower scattering medium (SR = 3.61) is that we already had a confident result with the higher scattering medium with back excitation which performing the front excitation with lower scattering is not a must. In this case, the thickness of the scattering medium is 1mm. Using the same 415nm LEDs light source, the LEDs light source is placed at an angle from the front of the roughened surface glass. Since the position of the excitation source changed from right behind the fluorescence slide to in front of the scattering medium, the emission light from the fluorescence reduced significantly as some of the excitation sources will be reflected and scattered away from the fluorphores layer.

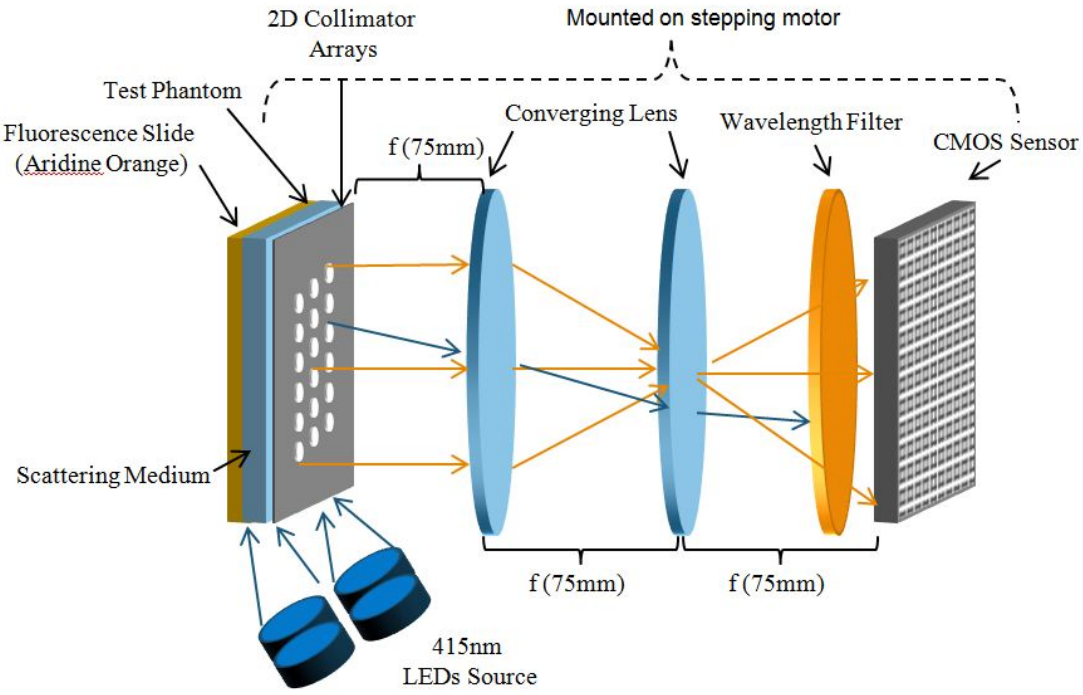

Figure 5-13: Experimental Setup with Front Excitation Illumination

With the same image technique as in the back excitation illumination, images are taken in a horizontal series manner which produced a stitched image at the end. As mentioned previously, we suspect the detectability of structures is defined by the spacing between the collimator holes. To enhance our observation, we will perform the imaging of the

structure with 2 different focal points where one is focused at the structure and the other is focused at the end of the collimator.

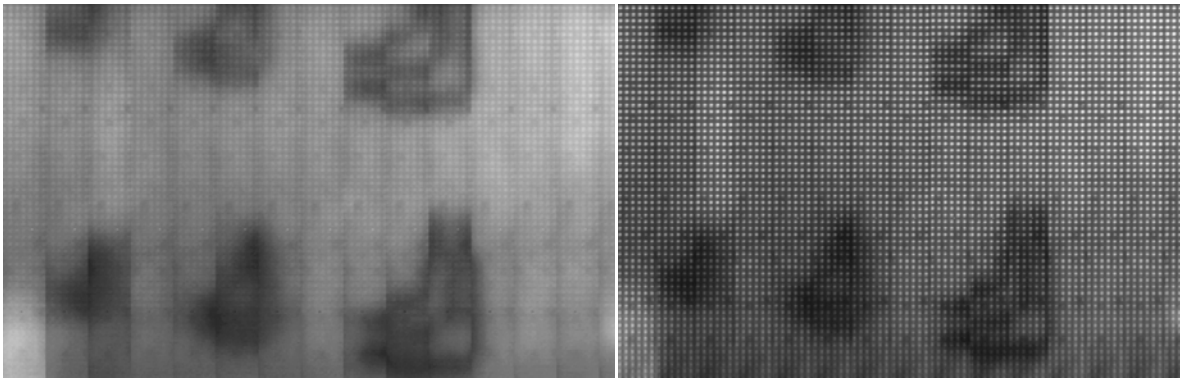

(a) **(b)**

Figure 5-14: Front Excitation Illumination ADI with Scattering Medium at SR = 328
(a) Focused at Structures ($MTF_{(200\mu m)}$=0.064, $MTF_{(300\mu m)}$=0.089, $MTF_{(400\mu m)}$=0.10)
(b) Focused at Collimator Arrays ($MTF_{(200\mu m)}$=0.27, $MTF_{(300\mu m)}$=0.27, $MTF_{(400\mu m)}$=0.29)

When the image is focused at the structures, Figure 5-11(a) shows that structures with 300µm lines and spaces are visible while the 200µm lines and spaces smallest structures visible but are hard to identify. Unfortunately, with the ADI system focused at the end of the collimator, similar results are produced as in Figure 5-11(b). These results showed that the 300µm detection limit of this ADI system with 10:1 aspect ratio is with a front illuminated excitation and a scattering medium of SR = 328. As explained previously, this amount of scattering is 15 times higher than a typical biological tissue of 1mm thick. Hence, with the actual biological tissue, we possibly are able to detect structures as small as 200µm. Furthermore, our analysis from the Monte Carlo simulation showed that we can increase the structures detectability by increasing the aspect ratio with a tradeoff of reduction in light intensity. This reduction can be compensated by increasing the exposure period of the image sensor. Lastly, to quantify these result, MTF of these images are calculated. Figure 5-11(a)'s $MTF_{(200\mu m)}$ is 0.064 and Figure 5-11(b)'s $MTF_{(200\mu m)}$ is 0.27.

In summary, with the use of 2D collimator array, we are able to image structures with different widths of lines and spaces in a scattering medium higher than typical biological tissues. Comparing the MTF of images, we discovered that changing the focal point of the image will significantly change the structures detectability of the images.

Table 5-1: $MTFs_{(200\mu m)}$ for ADI at Different Focal Position

Scattering Ratio (SR)	Modulated Transfer Function of 200µm lines/spaces ($MTF_{(200\mu m)}$)					
	Back Excitation Illumination Source			Front Excitation Illumination Source		
	Focused at the Structure	Focused at the End of the Collimator Holes	% Difference	Focused at the Structure	Focused at the End of the Collimator Holes	% Difference
3.61	0.27	N/A	N/A	N/A	N/A	N/A
328	0.094	0.12	21.67%	0.064	0.27	76.29%

Table 5-1 summaries the MTF of ADI images with different scattering coefficient and focusing position. It showed that the focal point of the ADI system affects the MTF of the image by at least 70%. When the scattering increases, the difference reduces as the amount of the light passes through the collimator decreases. This is important for us to carry on future studies on how to capture the image and what is the major factor that needs to be considered when performing ADI under these conditions. And how could we use the 2D-AFA towards the new solid phantom.

5.5 Chapter Conclusion

In this chapter, we showed the application of ADI on shallow scattering depth with fluorescence was explored. Although previous research has used ADI extensively in thick scattering medium with relatively small acceptance angle (< 1º), ADI in shallow tissue was explored here. From the Monte Carlo simulation, we found that with a relatively small aspect ratio (~10-20:1) could perform ADI at shallow tissue depths (~1-2mm). Applying the 2D collimator array on top of the scattering medium, ADI was performed as the array served as an angular filter by limiting the photon's pathway enters and exits the collimating tunnel. The resulting angular filtered image is produced at the end of the tunnels. Based on the simulation results in chapter 4, 10:1 aspect ratio provided a good performance on both angular filtration and image quality. Since we can detect 200µm structures with SR of 328, this shows that we preliminary achieved our goal of detecting the size of average tongue tumor tissue of 200-400µm. Hence, this shows that 2D collimating ADI can potentially used on this type of application. At the end, with the artificial fluorescence material, ADI has a superior performance on the image in shallow depth tissue. This experiment provided a backbone for a further study on the application of shallow depth ADI with actual biological tissues, e.g. collagen imaging.

In the next chapter, we will perform another type of angular filter, SpatioFrequency Filter on our newly developed solid, stable scattering phantom which showed in chapter 3. This allows us to study the application of ADI towards a 3D scattering media in complex structural dimension. Also, the feasibility of applying SFF ADI on fluorescence source.

Chapter 6: SpatioFrequency Filter ADI

In chapter 2, we discussed about the general configuration of SpatioFrequency (SFF) Filter ADI. And in chapter 3, we showed our newly developed solid stable scattering phantoms. Now, we want to use SFF on the new sample with both trans-illumination fluorescence and low coherence narrow wavelength source to see the impact of the imaging performance. Also, we also tested our SFF system with an aquatic creature, *Branchiostoma lanceolatum*, which has a modest scattering with internal structures. This test the ability of SFF when seeing through complex 3D scattering media.

6.1 Three Dimension Intralipid Infused Agar Phantom

Using the similar fabrication process which discussed in chapter 3, we also created another 3D scattering phantom. This 3D scattered medium was a V-shaped double wedge form as shown in figure 6-1. This wedge has a rectangular base in 3cm X 4cm with a height of 5mm. The wedge shape provides changes in thickness of scattering medium which results in its scattering level increases along the axis which creates a complex scattering medium. This replicates a common problem in living creatures – very large variations in scattering levels due to changes in scattering thickness. The scattering agar is calibrated to have a scattering coefficient of $200cm^{-1}$ at 630nm wavelength and anisotropy factor of 0.80. These values are similar to human skin tissue where it can be reused for our further research on human soft tissue scattering (1). Using the technique in chapter 3, first we created the outer rim of a clear polyester container. Then, a mould was placed inside the container to help forming the wedge scattering agar with a resolution target (figure 6-2) placed underneath. The resolution target has sizes ranging from 200µm to 1000µm lines and spaces. Finally, the top plastic layer sealed the structure and was polished with a chemical polish. The final encapsulated 3D complex intralipid-infused agar scattering structure is shown in figure 6-3 as proposed. We can see that the encapsulation does not destroy the agar wedge structures. Thus, the encapsulated intralipid-infused agar technique is not limited to only flat 3D layers structures. As a result, we can virtually create any shapes within the encapsulation. An important advantage of this wedge is the same structure has a huge range in its scattering ratio, which can be calculated simply by the location on the wedge being imaged. This allows extensive testing on one sample.

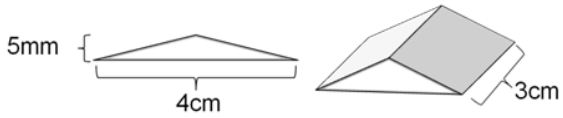

Figure 6-1: 3D Scattering Wedge

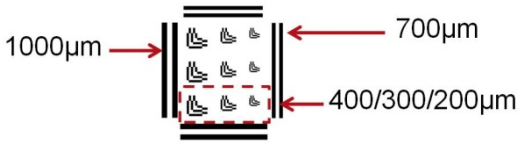

Figure 6-2: Resolution Targets

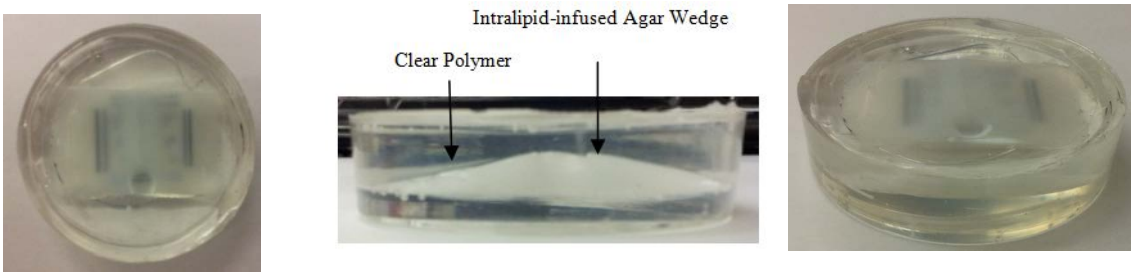

(a) (b) (c)

Figure 6-3: Encapsulated 3D Wedge Scattering Structure
(a) top view (b) side view (c) 45° angled view

6.2 SpatioFrequency Filter ADI Experimental Setup on 3D wedge

As discussed in chapter 2, a simple SFF filter is formed by a combination of a converging lens with a focal length (*f*), and a small aperture holes in few hundred microns range. This combination creates an acceptance angle for the scattered photons filtration. Figure 6-4 shows the experimental setup for imaging the 3D wedge phantom.

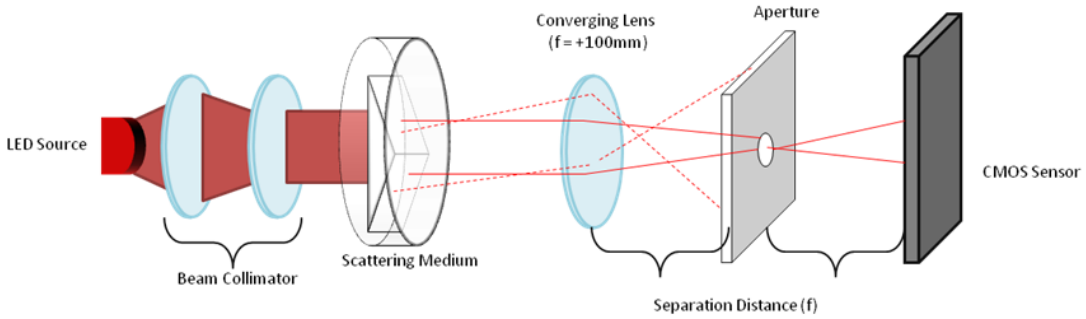

Figure 6-4: SFF system with lens, aperture, and imaging sensor

Unlike previous SFF ADI work which used a coherent light source, we used a LED source which is incoherent light with a narrow wavelength band (410nm ± 10nm and 639nm ± 10nm) but is emitting in approximately 10º angle (27) (28). To apply SFF ADI, we need to have a collimated light sources ensure a proper filtration where the scattered

photons are expecting to have an angular deviation from the collimated ballistic photons. Hence, a lens system is created to collimate our LED sources. This lens system consists two lenses, a diverging lens with f = -25mm which placed 40mm from the LED and a converging lens with f = 50mm which placed 55mm from the diverging lens. As a result, the beam is expanded into a 2.5cm circular beam. The collimated beam then illuminates our 3D scattering medium which is held vertically as an optical element. This cannot be done with the non-encapsulated intralipid-infused agar as the agar will slip out from the container rather quickly. After the scattering medium, it is our SFF ADI setup as discussed in section 2.3.

The SpatioFrequency Filter setup in this experiment is created by a 300μm aperture and a +100mm lens. This produces an acceptance angle of ≈ 0.172°. And the camera sensor placed at the converging lens' focal length to aperture. Since the SFF provided a full view image filtration, unlike other ADI techniques, images can be captured in real-time at rates which limited by the CMOS Sensor. Inherently, as the aperture is introduced into the system, the total amount of light that reaches the CMOS Sensor is reduced. Hence, a long exposure would be required for a highly scattered medium.

6.2.1 Illumination Source Considerations

One of the advantages of ADI is its compatibility with many illumination sources, regardless of the source's wavelength, coherence length or type. Moreover, the light source selection becomes more complex in real-life biological sample imaging. The foremost consideration in biological imaging source wavelength spectrum due to its impact on the scattering level of the sample. A long wavelength light source (such as 630nm) is preferable because the scattering effect within the biological sample increases as the wavelength of the illumination source decreases (10). However, there is an upper bound to the illumination source's wavelength beyond the visible light due to upper detection limit of the silicon imaging sensor (1.1μm).

The other factor that has to be considered is the coherence length of the light source. The coherence length of a laser is defined as the distance over which a light source can maintain its coherence or spatio and temporal uniformity. In previous ADI experiments, the coherence length is not considered because the light source's coherence does not directly impact the quality of the ADI imaging system. However, this becomes a concern

in 3D scattering structures. The uneven depths across the scattered medium can lead to the possibility of interference in the resulting images when the coherence is longer than the dimension of the structure. This interference effect provides additional findings about the specimen which cannot be obtained otherwise, specifically the contour information of the sample (see section 6.2.2). Conversely, a light source with a shorter coherence length can provide more structural data of the phantom. Hence, using a controlled 3D scattering structure helps us understand the results.

6.2.2 Narrow Band Incoherent LED Source - 415nm and 630nm

In this experiment, two different light sources are investigated. They are 10mW 415nm blue LED (28) and 5mW 630nm red LED sources (27). These light sources can provide a thorough study of how wavelength and coherence length affect the effectiveness and quality of 3D complex scattering wedge, and the tradeoff between the differences in the light source's coherence length. Using multiple light sources on the same scattering structure allow us to study the impact of wavelength dependent tissue scattering. With multiple thickness, the scattering level increases exponentially. Hence, we can see how it changes the SFF ADI results.

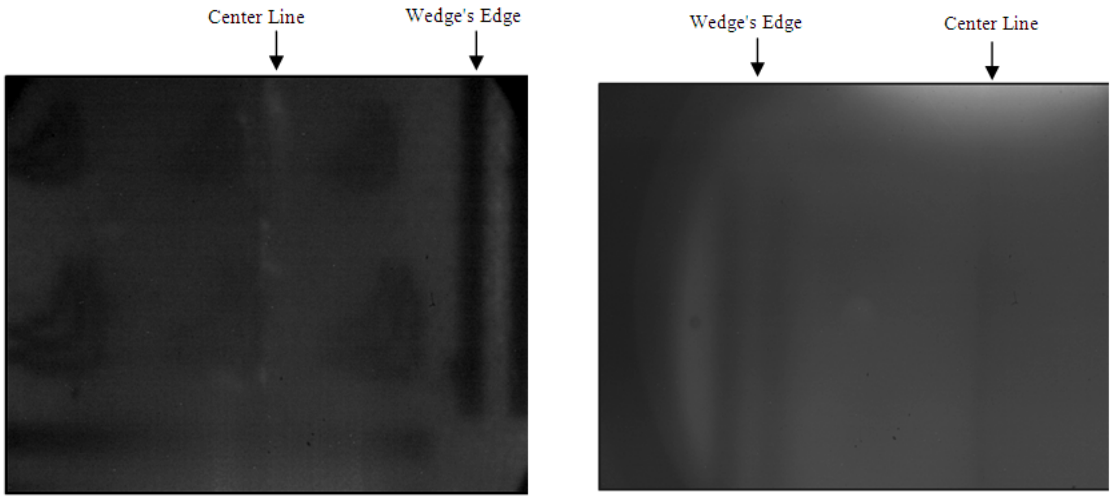

Figure 6-5: SFF ADI image with (a) 630nm LED source and (b) 415nm LED source

Figure 6-5(a) shows the SFF ADI result using 630nm red LED source. At this wavelength, we can clearly detect the 300µm structures (figure 6-2) at the center line which has scattering thickness of 5mm. On the other hand, when we switched to the 415nm blue LED source, we can only detect the structure at the edge of the scattering

wedge. Looking at the scattering level for these 2 wavelengths, the scattering coefficient increases from ~200cm^{-1} for 630nm to ~600cm^{-1} for 415nm which measured with the technique we showed in section 3.6. At the 5mm thickness, the scattering ratio increases from 4.851 x 10^{8} for the red light to 1.142 x 10^{26} for the blue light which is 2.35 x 10^{17} times increase. The range of scattering for these wavelength is summarized in table 6-1. This enormous increase in scattering ratio reduces our SFF ADI system's imaging capability. Calculating the scattering level at the edge of the wedge at the 415nm, it gives us a scattering ratio of 2.649 x 10^{10} which is equivalent to 6mm of scattering thickness at 630nm. This shows that the reason why we could not detect the structures in 415nm, which is due to the extreme high scattering induced by the short wavelength (415nm). Furthermore, with this solid, long term scattering medium, we can perform multiple scattering level analyses on same 3D structures by only changing the illumination source. This is extremely beneficial for experiments as we do not need to recalibrate for a new scattering phantom overtime as organic scattering phantom degrades rapidly.

Table 6-1: Scattering Coefficient and Scattering Ratio at different Wavelengths

Wavelength (nm)	μ_s (cm^{-1})	Scattering Ratio at different thickness		
		At the edge (≈1mm)	At 2.5mm	At 5mm
415	~600	1.628 x 10^{5}	1.068 x 10^{13}	1.142 x 10^{26}
630	~200	5.460 x 10^{1}	2.203 x 10^{4}	4.851 x 10^{8}

Also, using a small acceptance angle of 0.172º, we clearly able to image through a 5mm thick scattering phantom with 630nm incoherent LED source. On the other hand as noted in section 2.3, if we further reduce the aperture size of our SFF ADI setup, even though it reduces the acceptance angle but diffraction limit starts to take place. Therefore, there is a trade-off between angular filtration and imaging quality.

6.3 SpatioFrequency Filter ADI on Small Aquatic Creature

Previously we showed that the SFF ADI is able to image through a 3D complex scattering phantom with low power, low coherent LED source. Now we take a step further to apply SFF ADI on a small aquatic creature which has a modest amount of scattering in relatively thin tissue. A small aquatic creature (figure 6-7), *Branchiostoma lanceolatum*, is selected for performing ADI on 3D structures. The reason we chose this dead creature is because it has a modest amount of scattering with relatively thin

scattering thickness (~around 5mm at the maximum point), has complex internal structures at different part of the body, has a good water compatibility which allows test on refractive index matching on material/surface, and is readily available in fish markets providing fresh sample for the experiments and does not degrade quickly.

This creature has an elliptical 2D cross section with a maximum radius of 2.5mm and a length ranges from 5cm to 8cm. Since it has a modest amount of scattering with internal structures, it serves as an ideal candidate for back-illuminated ADI. The lancelet, *Branchiostoma lanceolatum*, is placed in a parallel-walled glass container filled with deionized (DI) water and suspended by thin copper wire loops which hold the creature in mid-water as in figure 6-6. By filling up the container (refractive index of 1.5) with DI water (refractive index = 1.33), reduces the refractive index changes between the lancelet (human soft tissue refractive index ranges from 1.39 to 1.452) (29) and the surrounding (e.g. air with refractive index = 1), hence this improves the ADI imaging quality as the exiting photons have lesser chance refracted away from the SSF filter. Also, DI water, serves as a surface matching solution which eventually reduces the surface scattering. We will also perform ADI without DI water to analyze the impact of surface scattering to our system.

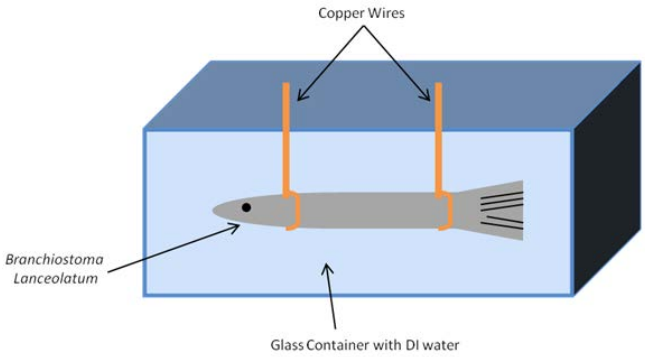

Figure 6-6: Illustration of Lancelet's position in the DI water container

Figure 6-7: Lancelet in back illuminated white light using simple camera setup

The most common imaging method of any aquatic creature is by using a regular camera, illuminated by a white light source. In Figure 6-7, we can see that using the regular camera setup to image our specimen, *Branchiostoma lanceolatum*, the creature appears to be nearly opaque and solid, clearly outlined in the black background with only some superficial surface patterns and features being visible. Although it makes a striking image of the sample, we are only able to obtain little additional information about the internal structure or contour. By using ADI, we hope to provide a simple method in obtaining information that gives a structural understanding and 3D profile of this aquatic specimen.

6.3.1 SFF ADI on Small Aquatic Creature Experimental Setup

For this experiment, we used 3 different types of light source for our imaging illumination. First, a high powered incoherent white light source with wide spectrum and modest collimation is setup for full field illumination. Next, a 20mW Nd:YAG second harmonic laser at 532nm with 40x beam expander to produce a Gaussian spot size of 1.2cm was used. The resulting Nd:Yag beam size will be sufficient for illuminating a portion of the bio-creature, for example the head section. Lastly, a single mode 3mW diode laser at 780nm with a Gaussian spot size of 2cm after a 40x beam expander is also applied to illuminate a section of the creature. The purpose of using multiple wavelengths and a white light source is that multiple wavelengths take the advantage of scattering is heavily related to wavelength. With multiple wavelengths, we can extract different scattering and/or structural information of scattering medium.

Furthermore, ADI does not rely on wavelength which means imaging procedures for all wavelengths are essentially the same. As a result, different spectral images can be achieved within one system. A +75mm converging lens with different apertures

(500µm/300µm) placed at the lens' focal length formed the SFF with acceptance angle of ~0.38° or ~0.23° and the image sensor located at 2 times the lens' focal length for the imager creates the ADI system as in figure 6-8. This system is covered by a container that blocks out ambient light. Subjective criteria were used to determine optimum exposure setting to avoid image saturation. As discussed in section 2.3, we need to keep the distance between the SFF system and the container in minimum.

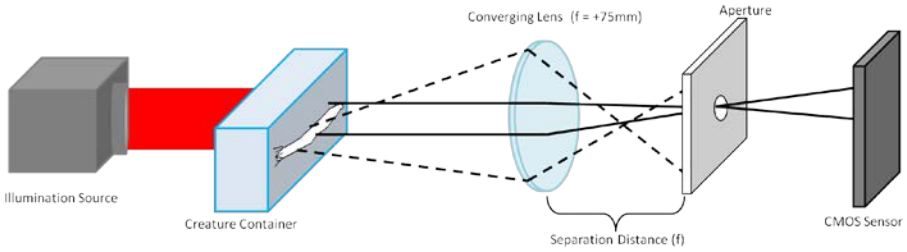

Figure 6-8: SFF system with aquatic creature, lens, aperture, and imaging sensor

6.3.2 Experimental Results of SFF ADI on Small Aquatic Creature

Two portions of the aquatic specimen, the head and the tail, are imaged in this experiment. These areas are chosen because of the complex structure and contour of the head area (the thickest) and the transparency and thinness of the tail area, which are contrasting qualities. The experimental results are separated into three sub-sections: the first section focuses on images using incoherent light source, the second section focuses on images using light sources with different level of coherence, and the last section focuses on the effects of coherence on samples with varying thicknesses.

6.3.2.1 Incoherent Light Source - White Light

One of the light sources used in this experiment is the broad-band white light incoherent but nearly collimated source. This source is modified from a slide projector lamp with a lens to slightly collimate its output as in figure 6-9. In the first order of experiments, we investigated the necessity of index matching. The aquatic specimen imaged was suspended in air or within a glass container filled with DI water as in figure 6-6. Figure 6-11 and figure 6-12 show the images of the creature suspended in air and immersed in water. These images have been processed to show only the red wavelength spectrum.

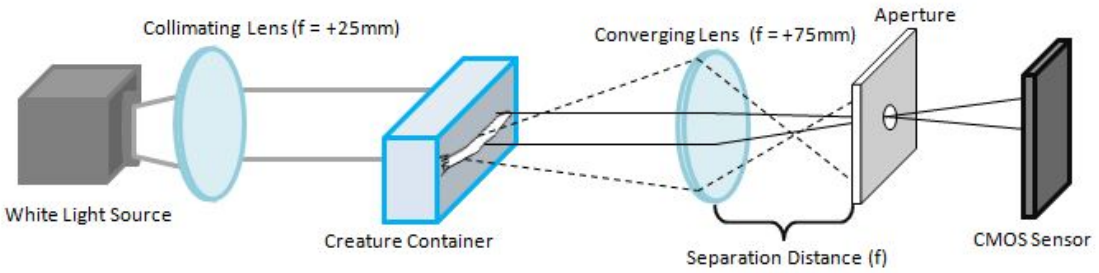

Figure 6-9: Illustration of SFF ADI with white light source

Earlier in this chapter, we commented that the wavelength of the light source has a significant impact on the scattering level of a biological tissue. Next, we are going to investigate the effect on scattering level between a shorter wavelength (blue spectrum end) and a longer wavelength (red spectrum end). Figure 6-13 shows the images of the specimen's head area with only the blue wavelength spectrum (~480nm) (figure 6-13(a)) and only the red wavelength spectrum (~720nm) (figure 6-13(b)).

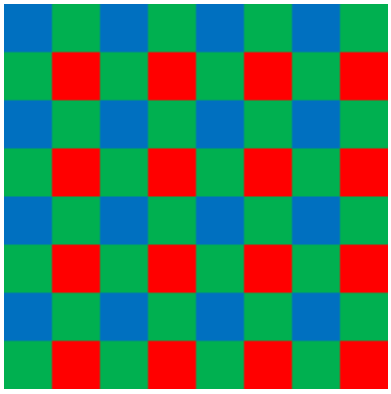

Figure 6-10: Bayer filters configuration

The two images above originated from one single image, but they are processed to show only the blue and the red wavelength spectrum respectively using Matlab image processing functions. This spectral selection is done with the aid of the Bayer filters (figure 6-10) in the imaging sensor which allows a single illumination image to be separated in the red, green, and blue spectra. Before we analysis the impact of spectra difference in scattering tissue, we compare the refractive index matching results.

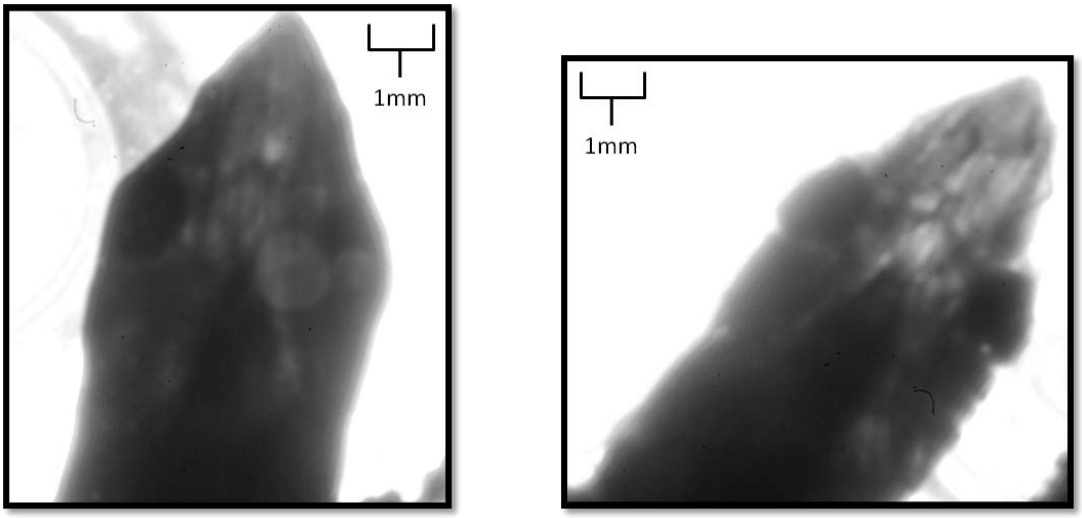

(a) (b)

Figure 6-11: Images of *Branchiostoma lanceolatum* - Head Area using white light (red band) (a) Specimen suspended in air (b) Specimen placed in water

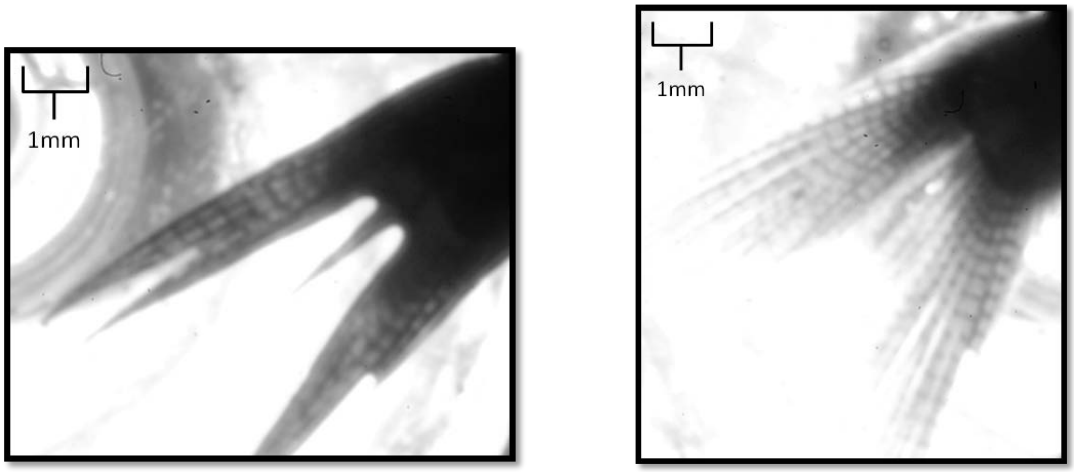

(a) (b)

Figure 6-12: Images of *Branchiostoma lanceolatum* - Tail Area using white light (red band) (a) Specimen suspended in air (b) Specimen placed in water

The images above demonstrate that images are not greatly impacted by the difference in refractive index. A small improvement can be observed when placing the specimen in a glass container with water over that suspending it in air. More structural information can be identified in the images with the specimen immersed in water. In figure 6-11(b), by immersing the specimen in water, the eye area is more defined when compared to Figure 6-11(a) where the specimen was suspended in air. The same observation can be made on the tip of the head for the images in figure 6-11(b).

Similarly, for the images on the tail (figure 6-12(a) and (b)), the cartilage of the tail is more apparent and have better contrast in the one placed in water as compared to the

sample suspended in air. The level of details is better represented in the image with the specimen immersed in water. This is likely because of the flat surface of the glass container and the water acting as an index matching buffer for the aquatic creature. As a result, all the subsequently images presented in this section are of the aquatic specimen immersed in water within a glass container. Also, comparing the images with SFF and without SFF, we are clearly seeing a lot more details. With the regular camera (figure 6-7), we can only see the eyes and the outline of the head section. When imaging with SFF ADI, we are clearly seeing more internal structures within the head (figure 6-11). After the refractive index difference analysis, we now discuss how the different wavelengths is beneficial to imaging a scattering medium.

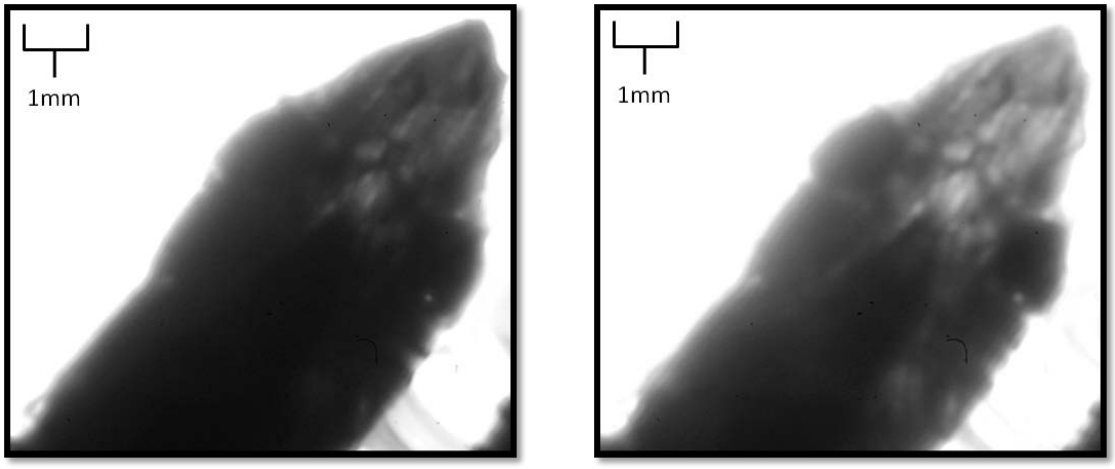

(a) (b)

Figure 6-13: Images of *Branchiostoma lanceolatum* – Head area
(a) Image shown in blue wavelength spectrum only (b) Image shown in red wavelength spectrum only

Using the same image but filtering out individual spectra, we can clearly see that the image at the longer wavelength (red) in figure 6-13(b) contains much more structural information than the image at the shorter wavelength (blue) in figure 6-13(a). The intensity difference between the two images demonstrates that less ballistic and quasi-ballistic photons are present in the blue range due to the much higher scattering level at the shorter wavelengths. This is as expected because as the scattering level increases, less non-scattered photons are present while the number of scatted photons remains approximately the same.

When looking at the head section in the blue (figure 6-13(a)) and the red (figure 6-13(b)) image, the light intensity (78 of 255 level in blue color and 119 of 255 level in red color) difference reduces the constructive information of the sample in the blue band. One

important detail to note from the images taken with the white light source is that no interference is present to distort the images. This is an advantage of incoherent light sources in addition to its potential in producing multi-spectral images from one original image.

6.3.2.2 Coherent Sources – 2nd Harmonic Nd:Yag Laser & 780nm Laser Diode

In this section, we investigated the effects of the second harmonic Nd:Yag laser at 533nm and the 780nm laser diode as illumination sources for the aquatic specimen. They each have different coherence length with the second harmonic Nd:Yag laser having a longer coherence length (roughly 14cm) than the 780nm laser diode (few mm). The beam quality of the second harmonic Nd:Yag laser is also superior to the 780nm laser diode. In addition, the second harmonic Nd:Yag laser source has a much higher output power than the 780nm laser diode; thus, the images using the second harmonic Nd:Yag source are expected to yield a shorter exposure than the 780nm laser diode.

Figure 6-14 shows images of the specimen under second harmonic Nd:Yag laser and 780nm laser diode.

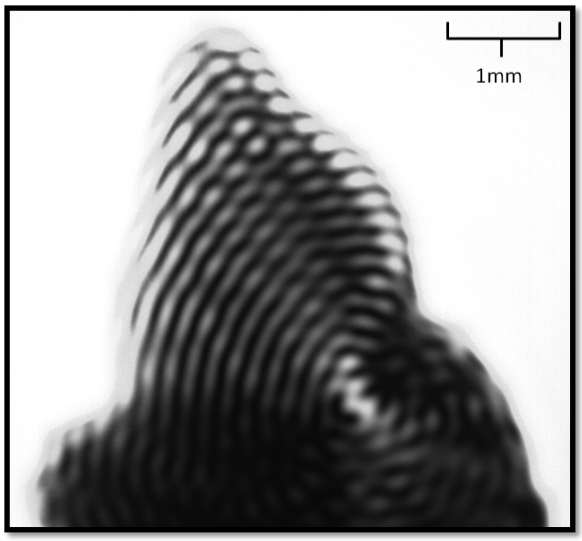

(a)

(b)

Figure 6-14: Images of *Branchiostoma lanceolatum*
(a) Second harmonic Nd:Yag laser at 533nm (b) 780nm laser diode

From the above images, we can clearly see the interference pattern under coherent light sources regardless of the level of coherence. And this pattern is not from the sample container which we will discuss in the next section. In the image with the second harmonic Nd:Yag light source, the interference pattern is much more pronounced than the image with the 780nm laser as illumination. From these two images, we can infer that there is a correlation between the coherence lengths with the severity of the interference pattern. The interference pattern distorts any structural information we can observe from the images. However, these inference ring patterns can potentially contain the contour information of the specimen. Note that the SFF has been found to be very prone to the interferences (4) in previous research as the coherence of the light source

especially laser sources. In future, we would like to reduce the interference from using a laser source by reducing the coherence of the laser. With a low coherent laser source, SFF ADI result could be benefited by the monochromatic of laser which can be targeted on specific tissue structures while minimize/remove interference pattern in the image.

6.3.2.3 Coherence Effect on Uneven Thickness Sample

In the previous section of experiment results, we suggest that the interference pattern is the result of the changing thickness across the aquatic creature. We are now going to further test on this theory using two smaller containers submerged within the sample containers. The illumination source used was the 780nm diode laser. The two containers are a 1cm by 1cm rectangular container and a 1cm diameter circular test containers. By imaging these two structures within the original sample container, we can show if the changing thickness across the sample is the reason for the interference pattern. This change introduces the least amount of impact to the system but significantly simplifies the complexity of the imaged subjects. Figure 6-15 shows the two images with the rectangular and circular containers. In the image of the rectangular container, we can observe nearly no interference, while in the image of the circular container, a significant amount of interference can be detected. The near parallel walls of the rectangular container obviously do not induce much interference pattern, unlike the changing thickness or contour of the circular container. This further validates the theory that uneven thickness of a sample along with a coherence light source result in interference patterns in images.

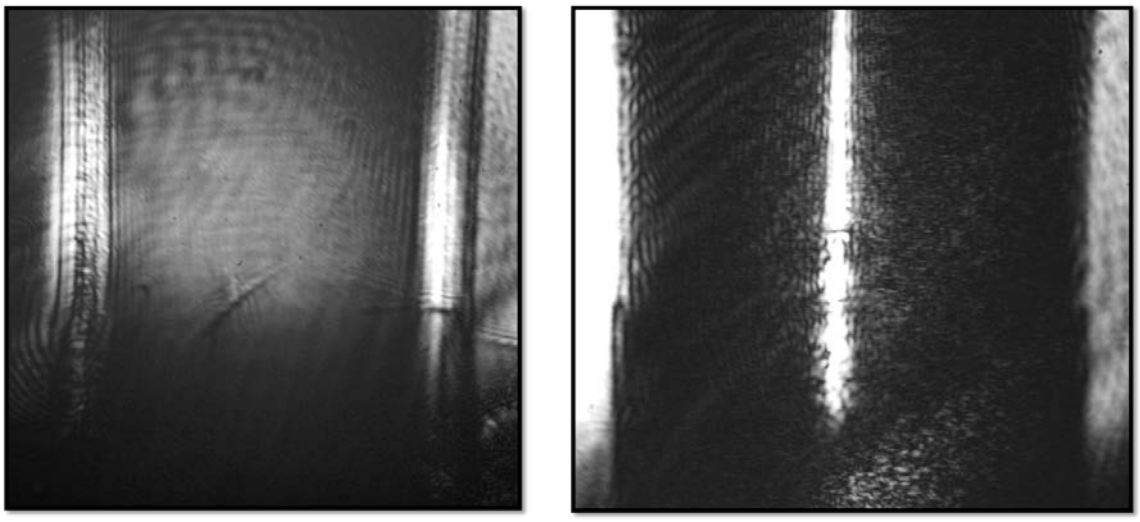

(a) **(b)**

Figure 6-15: Images of containers (a) Rectangular (b) Circular

Comparing these images with the 3D scattering wedge pictures, it clearly shows the interference generated by the coherence of the light. When using a low coherent source such as LED, the interface pattern disappears. In contrast, using a coherent light source, interference effect dominate in the images.

6.4 Chapter Conclusion

In this chapter, we created a 3D complex scattering phantom (wedge shape) using encapsulated intralipid-infused agar technique. This shows that we can virtually create any scattering structures regardless of it dimension and with multiple level of scattering layers. Also, SFF ADI can be applied towards this new type of scattering phantom which allows us to improve our SFF imaging technique on 3D scattering structure. Using multiple wavelength (415nm and 630nm) LED sources, we observed the relationship of scattering level and wavelength. Also using the 630nm LED source, we are able to image through 5mm thick scattering structure with resolution of 300μm lines and spaces.

Besides seeing through the 3D wedge scattering phantom, we also performed ADI on imaging an aquatic creature, *Branchiostoma lanceolatum*. Regular imaging method of such aquatic specimen is not able to provide any internal structural or contour information of the specie. On the other hand, with ADI, we see the internal structures in different part of the aquatic creature with an incoherent white light source. In addition, using a coherent source with SFF ADI can lead to a severe interference pattern distorting any internal structural information of the sample, but provides information to deduce the thickness of the sample.

The coming chapter will be the conclusion for this thesis as well as possible future work to enhance this system.

Chapter 7: Conclusion and Future work

This chapter presents a summary of the thesis, along with recommendations for future work in this research area.

7.1 Overall Summary

In this thesis work, we discussed about the concepts of Angular Domain Imaging (ADI) which it performs scattered photons filtration based on photon's trajectory. 2 ADI filters (2D-collimating arrays and SpatioFrequency Filter) have been introduced in chapter 2. These filters have different physical shape and component but they both filter scattered photons by limiting the range of allowed photon exit angles.

As intralipid has been used extensively in tissue scattering research, we target creation of a solid, long term stable tissue phantom. This phantom is aimed to mimic the soft human tissues such as skin. In chapter 3, we first created a solid scattering material via an infusion of intralipid into agar. Although this solid scattering medium produces a homogenous scattering, it has several problems. First, it is temperature prone. When the temperature increases, the heat melts agar which makes it slip out of container. Second, it is humidity sensitive. Water evaporates from the solid overtime which results in a paper thin material and peels itself away from its container. Even with this scattering agar extends its usable life time from less than a day for liquid intralipid to around 3 days for intralipid-agar, these inherent problems raise difficulties when handling/transporting the scattering phantom.

To further extend the intralipid-infused agar's longevity, we created a new technique to properly protect the delicate agar layer. This technique is to seal the scattering agar away from the environment. Using a clear unsaturated resin, the intralipid-infused agar is completed encapsulated inside clear plastic. This plastic has no/very low absorption from UV (400nm) up to NIR (900nm). It is extremely useful to optical tomography where most of the experiment are conduct in this range of wavelengths. Besides encapsulating a layer of scattering medium inside the plastic, this new technique can also create multilayer tissue phantom. For example, as shown in chapter 3, we also embedded a fluorescence layer with the use of a fluorescence plastic slide, a resolution measurement targets with a thin layer of scattering agar (2mm). As a result, a 3-layers scattering tissue phantom is produced which mimic the fluorescence of collagen layer beneath the

epidermis with lifetime over 200 days or at least 49 times than the regular agar-intralipid structures. Furthermore, using this phantom, we can virtually mount the sample in any required orientation for different experimental system without damaging the scattering layer.

Since we want to understand the photons' behavior in fluorescence with a shallow scattering depth when applying ADI, we performed Monte Carlo Simulation as showed in chapter 4. Two different scenarios were simulated. One is a fluorescence point source emission which replicates the artificially injected fluorophores. And the other one is a fluorescence plane source with uniform emission (Lambertian). In actual tissue, the fluorescence has a low emission intensity which is not favorable for imaging. To improve the imaging quality, fluorophores can be injected to increase the fluorescent intensity in targeted areas. Next, a scattering layer with a scattering coefficient of $200cm^{-1}$, a g factor of 0.85, an index of refraction of 1.33 was placed on the fluorescence layer. The simulator (PTS) allows user to create any optical layers, optical components (such as lens, aperture, mirrors), scattering level and thickness, and image plane via a text-script based input. To produce an acceptable result, an enormous number of photons is required for each simulation. In this work, 60 millions photons were launched for each individual set. This requires a computer with high computation power to handle this large number of photons.

The ADI filter used in this simulation is a 2D-collimating array which has series of holes with 100μm diameter. This angular filter has an acceptance angle of 5.72° for 10:1 aspect ratio and 2.86º for 20:1 aspect ratio. Using 2 different angles, the simulated results allow us to decide which is the best angle where we will actually fabricate the filter in chapter 5. The simulation showed that with both the injected point fluorescence source and the plane fluorescence source, the best aspect ratio of this new 2D-AFA is 10:1. And it suggested that with the ratio, we can detect either the injected fluorophores, or the non-emitting line in the plane fluorescence source.

Next in chapter 5, we reproduced the simulation with an actual experiment. We used a fluorescent plastic slide with excitation spectrum centered at 415nm, and emission spectrum centered at 580nm. A chemically etched glass slide was used as a shallow scattering layer. The 2D-AFA fabricated by using a power argon laser drilling system to

drill holes with average 88µm diameter on a 0.85mm thick ABS plastic. Sandwiching the resolution measurement target in between the fluorescence plastic slide and the scattered glass, creates the scattering phantom for this experiment. Then the 2D-AFA is place right on top of it to perform ADI. Since this experiment conducted before the work of the encapsulated agar phantom, we did not perform 2D-AFA ADI on it. The experimental results showed that using this filter, either with front and back illumination, we are able to detect structures with 200µm lines-and-spaces at a SR of 328. This level of scattering is roughly a 2mm skin tissue layer. Hence, 2D-AFA shows confident results on fluorescence ADI with shallow scattering thickness.

At last in chapter 6, we performed SpatioFrequency filter ADI targeted towards multiple complex scattering objects (such as an aquatic create which calls *Branchiostoma lanceolatum*, a 3D scattering agar wedge, and a high scattering intralipid-infused agar). In this, we used multiple sources (incoherent white light source, Nd:YAG second harmonic laser: 532nm, diode laser at 730nm, 415nm 10mW LED, 630nm 5mW LED, and fluorescence source with emission peak at 520nm. We used bio-creature, the lancelet, as the test object, it has a modest scattering level in a relatively thin tissue of 5mm with different internal structures. Applying SFF ADI with incoherent white light source and the color filter (Bayer) in the camera sensor, we are able to see internal structures of the head and tail sections. On the other hand, when using a laser source, interference pattern dominates the picture. The interference is induced by the coherence of the laser source.

Using the LED sources (415nm and 630nm) to illuminate the 3D scattering wedge with SFF ADI, we showed the relationship of wavelength and scattering as longer wavelength has a low scattering level on the same sample. With the longer wavelength (630nm), we can detect a 400µm structures with 5mm of tissue thickness at μ_s = 200cm^{-1} (SR = 4.851 x 10^8). But we only see the 1000µm structures with 1mm thick tissue at μ_s = 600cm^{-1} (SR = 1.628 x 10^5) when illuminated by shorter wavelength (415nm). Furthermore, this showed SFF ADI can be applied towards 3D scattering sample and produce useable results.

Lastly, we introduced a new ADI filters. It calls Pinhole ADI. It applies the concept of pinhole camera where image is produced with a small pinhole which create a small

acceptance angle. This new filter is used for the encapsulated intralipid-infused agar with fluorescence slide and resolution targets. With a high scattering level of 17000 which is 850 times higher than human skin tissue of SR = 20, the pinhole ADI able to picture the 400µm target with MTF of 0.055. One downside with pinhole ADI is that it does not produce a high resolution image.

7.2 Future work

There are few ideas that we can further explore based on this thesis work. First, we showed the importance of having a solid, long term stable scattering tissue phantom. In future (currently underway), we want to fabricate a more sophisticated scattering phantom. For example, a scattering layer with fluorescence strip which created by R6G and intralipid infused agar to mimic blood vessels in epidermis. Hollow tubing, which filled with liquid, beneath the scattering layer to study the ADI performance on different refractive index materials. Or, multiple scattering layers with same scattering level but different absorption levels. In theory, there is virtually infinite ways to create scattering phantom using this new technique. With a complex, multi-layered scattering, absorption phantom, we could have a better representation of a targeted human tissue for example epidermis. Next, we could use this simulated human tissue towards different ADI systems to study the functional performance and constrains. Hence, this allows us to further improve our ADI systems.

Also, with the 2D-AFA we introduced in chapter 2, we would like to apply this filter towards our solid scattering phantom and study the imaging quality of it. Furthermore, a modification of the current SFF ADI can be investigated. This modification could be adding extra relaying lenses after the aperture. These lenses will create another layer of angular filtering before the photons actually hitting the imaging sensor. In principle, we can also combine the 2D-AFA with SFF ADI to reduce the interference as the interference pattern generated by one hole will be even out by another pattern where its location is offset to the other one.

7.2.1 Pinhole Camera ADI

To further investigate the potential of SFF, we have designed a new preliminary ADI filter which called Pinhole Camera ADI. This ADI filter has a simpler setup than the SFF by removing the converging lens element in the SFF system. The concept is based on the pinhole camera, which creates image by reducing the acceptance angle. This new

angular filter which performs filtering via a small aperture placed at a specific distance from the scattering medium (figure 7-1). The combination of distance and aperture size creates the acceptance angle for the angular filter. In this experiment, we placed the 300µm aperture 10cm away from the 3D complex scattering surface and the same CMOS sensor is at 5cm away from the aperture. The combination creates an acceptance angle of 0.143º which is slightly less than the SFF ADI we shown previously with θ_a of 0.172º. We would like to see how this new angular filter performs on a 3D complex scattering medium and the image quality compares to SFF ADI using the 630nm LED sources.

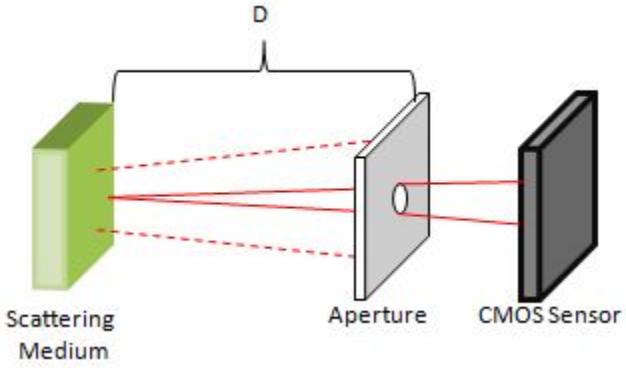

Figure 7-1: Pinhole Camera ADI Setup

Similar to SFF ADI, in order to produce a quality image, a collimated light source is required for Pinhole Camera ADI. Figure 7-2 shows the imaging result with Pinhole Camera ADI. Comparing this image to SFF ADI with $MTF_{(400\mu m)}$ = 0.15 at 2.5mm medium thickness (figure 6-5(a)), pinhole camera ADI creates a higher MTF image with $MTF_{(400\mu m)}$ = 0.18 at 2.5mm medium thickness (figure 7-2) but loses resolution as now we barely identify the 300µm lines and spaces structure. This shows the pinhole cameras has a lower sensitivity. Also, this new angular filter requires roughly 2 times longer exposure than SFF ADI in order to produce image with similar brightness. One reason for using the pinhole camera was because we noticed that the human eye actually sees much better through scattering mediums than a camera lens. This is because the small acceptance angle created by the pupil and the retina of the eye in some conditions.

There is a lot of similarities between the SFF ADI and Pinhole Camera ADI. The main difference is Pinhole Camera ADI does not have a lens placed in front of the aperture at focal point which makes it much poorer at gathering light. The existence of this lens

serves as light gathering element to the aperture. This increases the numbers of quasi-ballistic photon being captured. Thus, it increases the resolution limit of the system which explains SFF ADI able to detect the 300µm structure clearly.

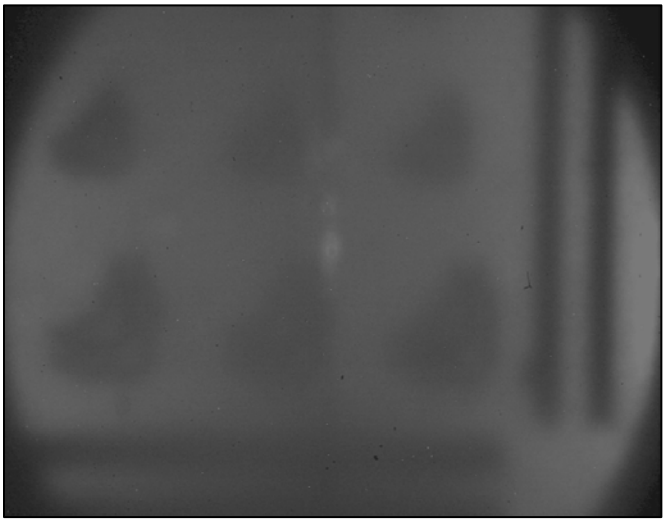

Figure 7-2: Pinhole Camera ADI Result with 630nm LED Source

Next, we will discuss the trans-illumination fluorescence ADI with Pinhole ADI system on the new encapsulated solid phantom.

7.2.2 Trans-Illumination Fluorescence Pinhole ADI

As noted in chapter 3, the fluorescing material used in this experiment has an excitation spectrum of 415nm, and emission spectrum of 530nm. A LEDs array operating at 415nm was used to provide the excitation source to the fluorescing slide beneath a 3mm thick intralipid infused agar with resolution targets range from 200µm, 300µm, and 400µm embedded underneath the 2mm thick scattering agar (figure 7-3). The scattering sample has a scattering ratio of 17000 with scattering coefficient at 240cm^{-1} and g factor of 0.8 at 532nm line which is equivalent to a 3.2mm thick human skin tissue. Comparing this scattering with actual human skin tissue, human skin has a much lower SR of 20 and μ_s of 200cm^{-1} for 1mm thick tissue (1). This shows that our scattering phantom is significantly higher than typical human skin tissue which may pose a problem of our imaging system due to very high scattering. Since this encapsulated phantom is our first actual working sample, we were still studying the relationship between the scattering in agar and the encapsulation. In future work which are underway, we will calibrate our solid scattering phantom as close to actual 1mm thick human skin tissue as possible. As

mentioned previously, an aperture with size of 500µm, 300µm, and 150µm is placed 10cm away from the scattering sample (figure 7-4). After the aperture, the CMOS sensor is positioned at 5cm away from the aperture which is limited by the casing of the CMOS sensor. In principle the location of the sensor may affect the imaging capability of the system.

Figure 7-3: Resolution targets with 200µm, 300µm, and 400µm lines and spaces

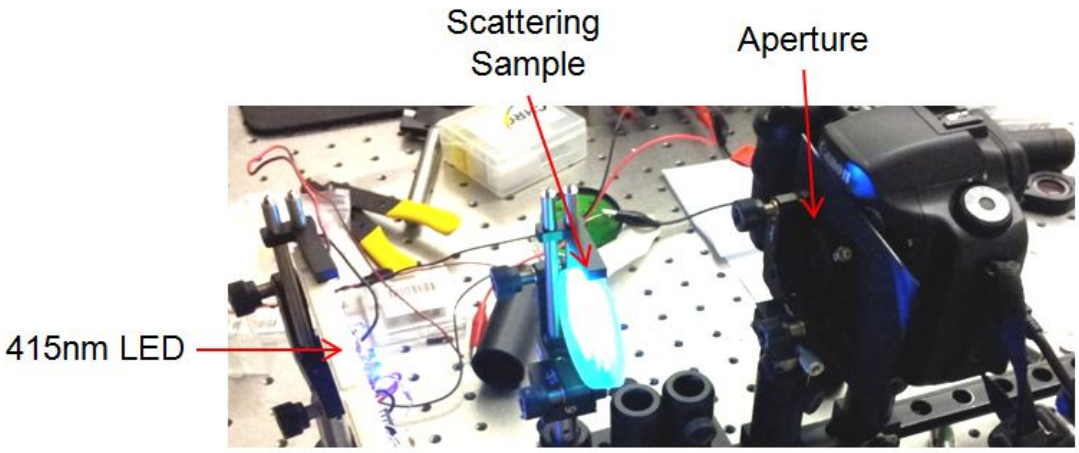

Figure 7-4: Actual Pinhole ADI Experimental Setup

To provide an evenly distributed excitation source, an array of 415nm LEDs configured to have 40mW combined power output which has a lambertian light spread characteristics. This type of light emission produces a good modeling on auto-fluorescence of collagen. Filtering out the excitation at the image sensor was performed by adding a HOYA Y-46 (Yellow) colored filter in front of the image sensor. This more closely resembles the fluorescence situations in collagen, with an excitation spectrum of 415nm and an emission spectrum of 520nm see chapter 3 and figure 5-5.

7.2.3 Pinhole ADI Experimental Results

To emulate a fluorescence layer, fluorescence slides were used as the fluorescent source in our experiments. The fluorescence slides used in this experiment had a green emission (FITC/GFP). In order to excite the fluorescence, a 10mW 415nm LEDs light source selected as an excitation source which gives a fluorescence emission peaks around 530nm. To maximize the excitation light intensity and illumination area, a series of 4 LEDs light sources formed a rectangular array for excitation. The fluorescence characteristic of the green emission fluorescence slide mimics the spectral response of the collagen layer which is embedded in the encapsulated intralipid-infused agar phantom.

7.2.3.1 Pinhole ADI with 500µm Aperture

Using a 500µm aperture, we created an angular filter with acceptance angle of 0.286º by using the formula [7]. Firstly, we tested this new system with only a fluorescence slide and the resolution targets to set the baseline for further measurement with the solid scattering phantoms. Figure 7-5 shows the result with only the resolution targets. It clearly shows that our Pinhole ADI system is capable of imaging structures down to 200µm lines and spaces. This served as our control which will be used to compare with the scattering phantom imaging results.

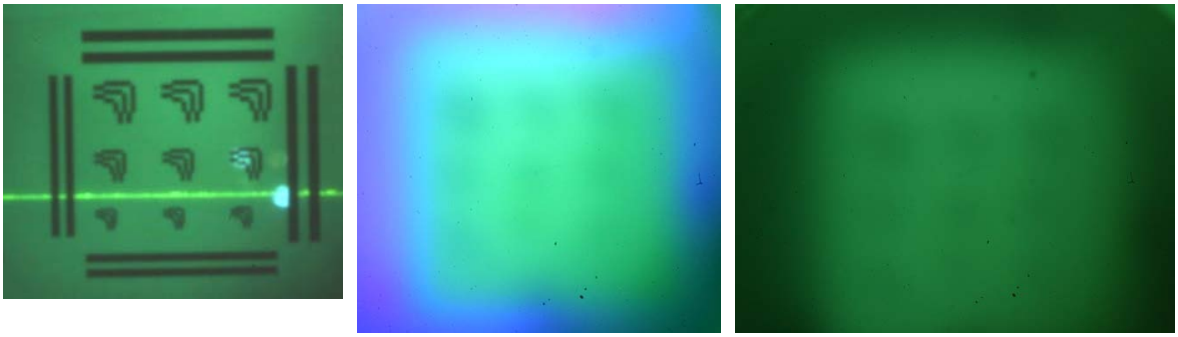

Figure 7-5: Fluorescence Pinhole ADI image with Resolution Targets

(a) **(b)**

Figure 7-6: 500µm Pinhole ADI image with a SR = 17000 (μ_s'=48.4cm^{-1}) sample
(a) Fluorescence without Excitation Filter
(b) Fluorescence with Excitation Filter

Figure 7-6 (a) and (b) show the different between fluorescence pinhole ADI images without excitation filtration and with excitation filtration. When the excitation filtered out by the color filter, we achieved an image similar to an actual fluorescence image which shows that our fluorescence solid tissue phantom behaves as expected. Since our newly created fluorescence scattering phantom has SR of 17000 which is 850 times higher

than actual human skin tissue (SR = 20), we only able to detect the 400µm L-shaped structures' locations with $MTF_{(400\mu m)}$ = 0.047. This is a much tougher phantom compare to the actual skin but our system still able to see through. Thus, with a lower scattering level, we are confident that this system able to image through the tissue and detect structures underneath. And this suggested that we need a more sophisticated angular filtration technique to improve the imaging results. Therefore, first we decrease the acceptance angle by reducing the aperture size to see the improvement of the images.

7.2.3.2 Result Comparison on Pinhole ADI with Different Apertures

At this high scattering level, let's compare the result captured via different aperture size. By reducing the size of the aperture, we are decreasing the acceptance angle. For this part of the experiment, we lowered the aperture size from 500µm to 300µm and 150µm to see the improvement of the pinhole ADI. First, we noticed when the aperture size is smaller with 300µm and θ_a = 0.172º, we have a higher $MTF_{(400\mu m)}$ of 0.062. As shown in figure 7-7(b), we can see all 9 structures location, while compare to figure 7-7(a), we can only see 6 structures. When further reducing the aperture size from 300µm to 150µm with θ_a = 0.086º, the field of view decreases as shown as the black circle in figure 7-7(c) and it does not improve the target location detection significantly with $MTF_{(400\mu m)}$ = 0.064. Furthermore, each time when we reduce the aperture size, it requires roughly 2 times the exposure in order to maintain the similar image brightness. This is due to the photons is strictly filtered by the small acceptance angle. At 150µm aperture, it requires an exposure longer than 30seconds. Also, with small aperture, diffraction limit begins to dominate which create another image degradation layer with minimum aperture size of 150µm (30). In theory, we can increase the field of view by moving the aperture close to the CMOS sensor which currently is limited by the sensor casing. At last, from previous experiments we showed that Pinhole Camera ADI can achieve a higher MTF image but with poor resolution. In future, we would like to investigate the Pinhole Camera ADI by adding extra optical components for example a focusing lens after the aperture to increase its light gathering ability and potential resolution improvement.

(a) **(b)** **(c)**

Figure 7-7: Pinhole ADI image on a SR = 17000 sample with aperture size of (a) 500µm (θ_a=0.286º) with $MTF_{(400\mu m)}$ = 0.055 (b) 300µm (θ_a=0.172º) with $MTF_{(400\mu m)}$ = 0.062 (c) 150µm (θ_a=0.086º) with $MTF_{(400\mu m)}$ = 0.064

With these experimental results on the Pinhole Camera ADI, we see that the depth of view of the optics system could be beneficial to ADI imaging where we may want to image a range of structures which lies underneath the surface at different depth. In future, we may want to create a testing phantom which the structures are placed at different thickness. Then, apply different ADI filters to it and compare the results base on the depth of view.

References

1. **R. Graaff, A. C. M. Dassel, M. H. Koelink, F. F. M. de Mul, J. G. Aarnoudse, W. G. Zijlstra.** *Optical properties of human dermis in vitro and in vivo.* 4, s.l. : Applied Optics, 1993, Vol. 32.

2. **Sinclair, Warren K.** *X-Ray-Induced Heritable Damage (Small-Colony Formation) in Cultured Mammalian Cells.* 4, s.l. : Radiation Research Society, Vol. 21, pp. 584-611.

3. **Chapman, Glenn H., et al.** *Angular Domain Image Detectability with Changing Turbid Medium Scattering Coefficients.* Burnaby : Proc. of SPIE, 2005, Optical Interactions with Tissue and Cells XVI, Vol. 5695, pp. 160-171.

4. **Chan, K. Y. Paulman.** *Angular Filters for Angular Domain Imaging Optical Tomography in Highly Scattering Media.* School of Engineering Science, Simon Fraser University. Burnaby : s.n., 2008. M.A.Sc Thesis.

5. **Brancaleon, L., Durkin, A. J., Tu, J. H., Menaker, G., Fallon, J. D. and Kollias, N.** *In vivo Fluorescence Spectroscopy of Nonmelanoma Skin Cancer. Photochemistry and Photobiology.* 2, s.l. : Photochemistry and Photobiology, 2001, Vol. 73, pp. 178-183.

6. **Pfeiffer, Nick, et al.** *Optical Imaging of Structures Within Highly Scattering Material Using a Lens and Aperture to Form a Spatiofrequency Filter.* Burnaby : Proc. of SPIE, 2008, Optical Interactions with Tissue and Cells XIX, Vol. 6854, pp. 68541D1-68541D12.

7. **Polly B.L. Tsui, Glenn H. Chapman, Rongen L.K. Cheng, Nick Pfeiffer, Fartash Vasefi, Bozena Kaminska.** *Spatiofrequency Filter in Turbid Medium Enhanced by Background Scattered Light Subtraction from a Deviated Laser Source.* s.l. : SPIE, 2009. Vol. 7175. DOI:10.1117/12.809592 .

8. **Chan, Paulman K. Y., et al.** *Multispectral Angular Domain Optical Tomography in Scattering Media with Argon and Diode Laser Sources.* Burnaby : Proc. of SPIE, 2007, Optical Interactions with Tissue and Cells XVIII, Vol. 6435, pp. 64350M1-64350M12.

9. **N. Pfeiffer, P. Chan, G. H. Chapman, F. Vasefi, B. Kaminska.** *Optical Imaging of Structures Within Highly Scattering Material Using a Lens and Aperture to Form a Spatiofrequency Filter.* s.l. : Photonics West, 2008, Tissue Optics, Laser-Tissue Engineering, and Tissue Engineering.

10. **Cheng, Rongen L. K.** *Angular Domain Imaging with Intralipid as Turbid Medium.* 2009.

11. **U Sukowski, F Schubert, D Grosenick and H Rinneberg.** *Preparation of solid phantoms with defined scattering and absorption properties for optical tomography.* 9, 1996, Physics in Medicine and Biology, Vol. 41, pp. 1823-1844.

12. **M Firbank, M Oda and D T Delpy.** *An improved design for a stable and reproducible phantom material for use in near-infrared spectroscopy and imaging.* 5, 1995, Physics in Medicine and Biology, Vol. 40, pp. 955-961.

13. **Marcia L. Vernon, Julie Fréchette, Yves Painchaud, Serge Caron, and Pierre Beaudry.** *Fabrication and Characterization of a Solid Polyurethane Phantom for Optical Imaging Through Scattering Media.* 19, 1999, Applied Optics, Vol. 38, pp. 4247-4251.

14. **E. Unsöld, R. Baumgartner, W. Beyer, D. Jocham and H. Stepp.** *Fluorescence detection and photodynamic treatment of photosensitized tumours in special consideration of urology.* 2, 1990, Lasers in Medical Science, Vol. 5, pp. 207-212.

15. **Ankri, R., Taitelbaum, H. and Fixler, D.** *Optical Technique for the Investigation of Light Transport within Irradiated Tissues.* s.l. : SPIE Photonics West, 2011. 7897.

16. **Cubeddu, R., et al.** *A solid tissue phantom for photon migration studies.* s.l. : Physics in Medicine and Biology, 1997, Vol. 42.

17. **Xia Cao, L.James Lee.** *Control of shrinkage and residual styrene of unsaturatedpolyesterresins cured at low temperatures: I. Effect of curing agents.* 6, 2003, Polymer, Vol. 44, pp. 1893-1903.

18. Fluorescence Reference Slides. [Online] Ted Pella, Inc. [Cited: August 3, 2012.] http://www.tedpella.com/histo_html/fluor.htm.

19. **Francisco del Monte, John D. Mackenzie, David Levy.** *Rhodamine Fluorescent Dimers Adsorbed on the Porous Surface of Silica Gels.* s.l. : American Chemical Society, 2000. Langmuir. pp. 7377–7382.

20. **Chapman, G. H., et al.** *Optical imaging of objects within highly scattering mediums using Silicon Micromachined Collimating Arrays.* s.l. : SPIE Photonics West, 2002. 4616.

21. **Chapman, Glenn H., et al.** *Enhanced Angular Domain Imaging in Turbid Media using Gaussian Line Illumination.* Burnaby : Proc. of SPIE, 2006, Optical Interactions with Tissue and Cells XVII, Vol. 6084, pp. 331-342.

22. **Chapman, G. H., et al.** *Angular Domain Imaging of Objects Within Highly Scattering Media using Silicon Micromachined Collimating Arrays.* 2, s.l. : IEEE, 2003, Vol. 9.

23. **Chapman, G. H., et al.** *Angular Domain Image Detectability with Changing Turbid medium Scattering Coefficients.* s.l. : SPIE Photonics West, 2005. 5695.

24. **David M. Harris Ph.D, Jay Werkhaven MD.** *Endogenous porphyrin fluorescence in tumors.* 6, 1987, Lasers in Surgery and Medicine, Vol. 7, pp. 467-472.

25. **Ina Pavlova, Michelle Williams, Adel El-Naggar, Rebecca Richards-Kortum, Ann Gillenwater.** *Understanding the Biological Basis of Autofluorescence Imaging for Oral Cancer Detection: High-Resolution Fluorescence Microscopy in Viable Tissue.* s.l. : American Association for Cancer Research, 2008. Clinical Cancer Research. pp. 2396-2404.

26. **Tsui, Polly.** *Angular Domain Imaging in Scattering Media with Background Subtraction, Multi-Spectral Sources, and Fluorescence.* School of Engineering Science, Simon Fraser University. Burnaby : s.n., 2011 Sping.

27. [Online] [Cited: August 3, 2012.] http://www.thorlabs.com/Thorcat/16600/LED630E-SpecSheet.pdf.

28. [Online] August 3, 2012. http://www.thorlabs.com/catalogpages/V21/1341.PDF.

29. **Kumar, Joseph M. Schmitt and Gitesh.** *Optical Scattering Properties of Soft Tissue: A Discrete Particle Model.* 13, 1998, Applied Optics, Vol. 37, pp. 2788-2797.

30. **Young, M.** *Pinhole Optics.* 12, 1971, Applied Optics, Vol. 10, pp. 2763-2767.

31. **Chen, Cheng, et al.** *A primary method for determination of optical parameters of turbid samples and application to intralipid between 550 and 1630nm.* 16, s.l. : Optical Society of America, 2006, Optics Express, Vol. 14, pp. 7420-7435.

32. **Nishimura, G., et al.** *Diffusing-wave absorption spectroscopy in homogeneous turbid media.* 1-3, 1996, Optics Communications, Vol. 128, pp. 99-107.

33. **PhD, Jacqueline Férézou, et al.** *Intralipid 10%: physicochemical characterization.* 11-12, 2001, Nutrition, Vol. 17, pp. 930-933.

34. **Sankaran, Vanitha, et al.** *Polarization Discrimination of Coherently Propagating Light in Turbid Media.* 19, s.l. : Optical Society of America, 1999, Applied Optics, Vol. 38, pp. 4252-4261.

35. **Staveren, Hugo J. van, et al.** *Light Scattering in Intralipid-10% in the wavelength range of 400-1100nm.* 31, Amsterdam : Optical Society of America., 1991, APPLIED OPTICS, Vol. 30, pp. 4507-4514.

36. **F. Vasefi, G. H. Chapman, P. K. Chan, B. Kaminska, N. Pfeiffer.** *Enhanced Angular Domain Optical Imaging by Background Scattered Light Subtraction from a Deviated Laser Source.* s.l. : Photonics West, 2008, Tissue Optics, Laser-Tissue Engineering, and Tissue Engineering.

37. **Chan, P. K. Y., et al.** *Angular Domain Optical Tomography in Scattering Media with Multispectral Diode Lasers.* s.l. : SPIE Photonics West, 2007. 6435.